Monthly Notices of the ROYAL ASTRONOMICAL SOCIETY

MNRAS 539, 1856–1878 (2025) https://doi.org/10.1093/mnras/staf622
Advance Access publication 2025 April 18

Radio AGN selection in LoTSS DR2

M. J. Hardcastle,[1★] J. C. S. Pierce,[1] K. J. Duncan,[2] G. Gürkan,[1,3] Y. Gong,[4] M. A. Horton,[5] B. Mingo,[1] H. J. A. Röttgering[6] and D. J. B. Smith[1]

[1]Department of Physics, Astronomy and Mathematics, University of Hertfordshire, College Lane, Hatfield AL10 9AB, UK
[2]Institute for Astronomy, Royal Observatory, Blackford Hill, Edinburgh EH9 3HJ, UK
[3]Australia Telescope National Facility, CSIRO Space and Astronomy, PO Box 1130, Bentley WA 6102, Australia
[4]School of Physical Sciences, The Open University, Walton Hall, Milton Keynes MK7 6AA, UK
[5]Astrophysics Group, Cavendish Laboratory, University of Cambridge, JJ Thomson Ave, Cambridge CB3 0HE, UK
[6]Leiden Observatory, Leiden University, PO Box 9513, NL-2300 RA Leiden, the Netherlands

Accepted 2025 April 7. Received 2025 April 1; in original form 2024 December 9

ABSTRACT

The wide-area component of the LOFAR Two-Metre Sky Survey (LoTSS) is currently the largest radio survey ever carried out, and a large fraction of the 4.5 million radio sources it contains have been optically identified with galaxies or quasars with spectroscopic or photometric redshifts. Identification of radio-luminous active galactic nucleus (AGN) from this LoTSS source catalogue is not only important from the point of view of understanding the accretion history of the universe, but also enables a wide range of other science. However, at present the vast majority of the optical identifications lack spectroscopic information or well-sampled spectral energy distributions. We show that colour and absolute magnitude information from the *Wide-Field Infrared Survey Explorer* (*WISE*) allows for the robust and efficient selection of radio AGN candidates, generating a radio AGN candidate sample of around 600 000 objects with flux density > 1.1 mJy, spanning 144-MHz luminosities between 10^{21} and 10^{29} W Hz^{-1}. We use the catalogue to constrain the total sky density of radio-luminous AGN and the evolution of their luminosity function between $z = 0$ and $z \approx 1$, and show that the typical mass of their host galaxies, around $10^{11}\mathrm{M}_\odot$, is essentially independent of radio luminosity above around $L_{144} \approx 10^{24}$ W Hz^{-1}. Combining with Very Large Array Sky Survey (VLASS) data, we show that the core prominences, radio spectral indices and variability of extended sources from the sample are qualitatively consistent with the expectations from unified models. A catalogue of the radio AGN candidates is released with this paper.

Key words: astronomical data bases: miscellaneous – catalogues – galaxies: active – radio continuum: galaxies.

1 INTRODUCTION

1.1 Why select active galactic nucleus?

Although the central supermassive black holes of galaxies must grow by accretion and merger so as to maintain the observed black hole mass/galaxy mass relation (Reines & Volonteri 2015), direct evidence for accretion comes only from the observation of active galactic nucleus (AGN) activity at one or more wavelengths. However, observational selection methods are essentially all biased in terms of the population of AGN that they can find. For example, selection of radiatively efficient AGN by their infrared (IR) or X-ray emission produces largely disjoint sets of galaxies in many studies (e.g. Hickox et al. 2009) despite the fact that we expect AGN to be luminous in both bands. Some of the selection effects in these populations are clearly expected in the context of unified models of AGN (Antonucci 1993), in which anisotropic extinction (due to the 'torus') affects the optical and X-ray emission of AGN from certain lines of sight. Other selection effects remain poorly understood.

One key selection effect in most wavebands is that the requirement for luminous radiation *directly* produced by the accretion on to the black hole selects, both theoretically (Narayan & Yi 1995) and observationally, for objects accreting at a rate above approximately 1 per cent of their Eddington rate, defined as

$$\dot{M}_{\mathrm{Edd}} = \frac{4\pi G M m_p}{\eta c \sigma_T},$$

where G is the gravitational constant, M is the black hole mass, m_p is the mass of a proton, η is a radiative efficiency factor, c is the speed of light, and σ_T is the Thomson cross-section. It follows that most AGN selection methods cannot even in principle select for accretion that is taking place at lower mass accretion rates than $\dot{M} \approx 10^{-2}\dot{M}_{\mathrm{Edd}}$. This imposes biases against detecting the accretion on to the most slowly growing or most massive black holes.

A crucial realization of the past couple of decades is that radio selection, while of course still biased, is not limited by an accretion rate bias in the same way. Radio emission from active galaxies is produced (dominantly in the high-luminosity population, among other possible

★ E-mail: m.j.hardcastle@herts.ac.uk

mechanisms that we will discuss in more detail later) by synchrotron emission from particles accelerated as a result of the evolution of relativistic jets generated close to the central supermassive black hole. It has long been known (Hine & Longair 1979) that only a fraction of radio-luminous AGN (hereafter radio AGN or RLAGN) show strong optical emission lines of the type associated with quasars or Seyfert 1 and 2 galaxies that participate in standard unified models. A consensus has now emerged (Hardcastle, Evans & Croston 2007; Antonucci 2011; Best & Heckman 2012; Hardcastle & Croston 2020) that some RLAGNs have all the apparatus of optical, IR, and X-ray emission directly from the accretion flow, and an obscuring torus, that we see with other AGN selection methods: these are the radiatively efficient (Hardcastle 2018a) or thermal (Antonucci 2011) RLAGN, and are observationally described as radio-loud quasars or high-excitation radio galaxies (HERGs). Others, which are generally the majority in samples selected without a strong bias to high radio luminosities, do not have any of the standard AGN apparatus but do still possess powerful jets: these are radiatively inefficient (Hardcastle 2018a) or non-thermal RLAGN (Antonucci 2011) and are observationally described as low-excitation radio galaxies (LERGs). Crucially, the Eddington ratios estimated for the different classes do appear to show a division at the expected level around 1 per cent Eddington (Best & Heckman 2012; Mingo et al. 2014; D24), although it is difficult to estimate these Eddington ratios accurately in the absence in many cases of accurate black hole mass and jet power estimates. Selection of RLAGN thus offers a view of accretion on to black holes at low Eddington rates that cannot be achieved in any other way, although at the cost of losing the ability to infer easily what those accretion rates actually are, since jet power does not necessarily relate closely to accretion rate (Mingo et al. 2014; Hardcastle & Croston 2020), is not easy to infer accurately from radio data alone (Hardcastle et al. 2019) and is almost certainly variable over the lifetime of a typical extended radio source.

If we choose to proceed in the face of these difficulties, it then becomes vital to understand how to select RLAGN from large extragalactic radio surveys. Such surveys are numerically dominated, at the faint end, by star-forming galaxies whose radio emission is largely due to cosmic rays accelerated in the intergalactic medium by supernovae related to recent star formation. In principle, the gold standard for selection of *radiatively efficient* AGN is spectral energy distribution (SED) fitting, which allows the fraction of radiation due to an AGN to be estimated from broad-band photometry (Calistro Rivera et al. 2016; Boquien et al. 2019; Best et al. 2023; Das et al. 2024) and therefore is not in principle biased against, for example, dust-obscured AGN. It could be argued that these codes will still not select faint AGN in bright galaxies, but in fact the lower Eddington limit for radiatively efficient AGN and the black hole mass/galaxy mass relation require a minimum bolometric luminosity for an AGN in a given galaxy[1] and so at least in principle with good enough broad-band photometry all radiatively efficient AGN can be selected in this way. Of course, in practice, and particularly for wide-area surveys, the high-quality broad-band photometry needed for SED fitting may not exist, and then it is necessary to resort to proxies of AGN activity such as optical spectroscopy, X-ray emission or radio or optical colours, which may not be reliable in all cases.

In some senses, the situation is far worse in the radio. Many, probably most, radio AGNs are not radiatively efficient, and precisely because the accretion rate is not limited, here the broad-band or monochromatic radio luminosity can take almost any value, limited only at the top end by the requirement that the accretion powering the jets should not be super-Eddington (Mingo et al. 2014). Arbitrarily, low accretion rates and thus jet powers appear to be able to exist. In addition, the radio emission from jets is not necessarily spectrally distinguishable from that due to star formation, and even when it is, good-quality broad-band radio spectral information is rarely available. The current most widely used method for selection of radio AGN is the 'radio excess' method, where the star formation rate of the host galaxy is estimated, directly or indirectly via some well-calibrated proxy, to allow an inference of the expected radio luminosity due to star formation; then the radio emission from an object that is significantly more luminous than this can be assigned to AGN activity (e.g. Yun, Reddy & Condon 2001; Kauffmann, Heckman & Best 2008; Hardcastle et al. 2016; Gürkan et al. 2018; Drake et al. 2024). This, however, clearly excludes AGN activity that produces emission that is similarly luminous to or less luminous than what is generated by star formation. These non-excess radio AGN can in general only be distinguished from star formation spatially, or on a statistical basis within a given population (e.g. Yue et al. 2024), and in many cases spatial decomposition would require observations of much higher resolution than are generally available in surveys (although see Morabito et al. 2022, 2025). Moreover, the radio-excess method requires a good star formation rate estimator from SED fitting or spectroscopy and, as with radiatively efficient AGN, these are not always available from wide-area surveys (see Smith et al. 2016).

As we have argued above, though, a census of accretion in the Universe is severely incomplete without including RLAGN, despite the fact that we currently cannot even in principle find all of them. RLAGN selection is not only important in itself, but permits a large amount of other studies of, among other things, AGN feedback and life cycles. The current best wide and deep radio surveys are those generated by the LOFAR Two-metre Sky Survey (LoTSS: Shimwell et al. 2017), which has released observations both of individual deep fields and of wide areas of the northern sky. This paper focuses on RLAGN selection in LoTSS.

1.2 RLAGN selection in the LoTSS wide-area survey

The current most sensitive LoTSS radio images are the first data release of the deep fields, covering the ELAIS-N1, Lockman Hole, and Boötes areas (Sabater et al. 2021; Tasse et al. 2021) and the second data release, DR2, of the wide-area survey (Shimwell et al. 2022). The deep fields benefit from excellent multiwavelength data and almost complete (95 per cent) optical identification (Kondapally et al. 2021) which has permitted SED fitting methods to be used to identify radio-excess RLAGN (Best et al. 2023; Das et al. 2024). The wide-area DR2 contains many more radio sources (over 4.4 million) but the optical data for this survey, where the *WISE* surveys and the DESI Legacy Survey are the deepest available in the mid- to near-IR and optical bands, respectively, are much shallower. Only 85 per cent of sources have any kind of optical identification, with the redshift fraction being even smaller (Hardcastle et al. 2023), while the far-IR data needed for high-quality SED fitting are completely lacking over most of the DR2 area. The key advantage of the wide-area survey is

[1] Very roughly, this fraction is simply given by the normalization of the black hole mass/galaxy mass relation together with the specific bolometric luminosity of a galaxy due directly or indirectly to stars, which is of order the solar luminosity. For the values quoted by Reines & Volonteri (2015), with a black hole mass of 0.025 per cent of the galaxy mass, the ratio between the AGN and galaxy bolometric luminosity can thus range between about 0.1 and 10 for Eddington ratios between 0.01 and 1. Fainter radiative AGN relative to their host galaxies can only exist in this model if their black hole masses fall substantially below the typical value measured by Reines & Volonteri.

that it has much better statistics, particularly for the rare luminous radio AGN, and so gives us a much more accurate overall view of the radio AGN population, at least in the local universe in which host galaxies and optical identifications can be found given our ancillary data. The wide-area LOFAR survey also benefits from synergies with other wide-area surveys, notably including the Very Large Array Sky Survey (VLASS; Lacy et al. 2020), which is less sensitive to steep-spectrum emission or extended sources but provides high sensitivity to flat-spectrum cores and higher angular resolution over all of the LoTSS coverage. The largest wide-area catalogue of RLAGN in general to date was provided by Hardcastle et al. (2019), based on the much smaller LoTSS DR1 release which contained only $\sim 325\,000$ sources in total.

In this paper, we aim to carry out radio AGN selection for the DR2 optical catalogue based on the data currently available. Our optical identifications are taken from Hardcastle et al. (2023, hereafter H23), who obtained optical/near-IR (hereafter simply ‘optical’) counterparts by a mixture of likelihood-ratio cross-matching for compact sources, more sophisticated algorithms for extended sources, and visual inspection. A minority of spectroscopic redshifts come from the Sloan Digital Sky Survey (SDSS), the Dark Energy Spectroscopic Instrument (DESI), and the Hobby-Eberley Telescope Dark Energy eXperiment (HETDEX), with the bulk of the redshifts being the photometric ones derived by Duncan (2022). Drake et al. (2024, hereafter D24) have recently cross-matched the optical identifications to sources from the SDSS spectroscopic sample, which allows spectroscopic classifications of that subset of our objects to be made. We begin by defining a radio sample and developing methods to separate RLAGN and SFG in our data set in the absence of complete spectroscopic data, using the D24 classifications as a starting point (Section 2). We then go on to check the consistency of the sources in this catalogue with expectations and with previous work in Section 3, before demonstrating its application to a number of science questions in Section 4. A summary and prospects for future work are given in Section 5.

Throughout the paper, we use a concordance cosmology in which $H_0 = 70$ km s^{-1} Mpc^{-1}, $\Omega_M = 0.3$, and $\Omega_\Lambda = 0.7$. Spectral index α is defined in the sense $S \propto \nu^{-\alpha}$ and for calculation of luminosities we take $\alpha = 0.7$ unless otherwise stated.

2 SAMPLE DEFINITION AND SELECTION

The process for RLAGN selection in LoTSS DR2 has steps in common with the DR1 AGN catalogue created by Hardcastle et al. (2019, hereafter H19), but is based on the DR2 optical ID catalogue from H23. A step-by-step description is given in this section of the paper.

2.1 Completeness and ID cuts

Initially we selected all sources with total flux density, after any source association, greater than 1.1 mJy and with an optical identification and redshift (corresponding to the FCOZ sub-sample in H19). The 1.1 mJy flux limit was taken from the 95 per cent completeness level given by Shimwell et al. (2022) and should ensure that we miss almost no point sources at this flux level that have optical IDs provided by H23. By chance, this total flux cut is almost exactly 10^4 times lower than that used by the widely used 3CRR survey (Laing, Riley & Longair 1983). It is important to note, of course, that there is also a strong surface brightness selection for this data set and that the completeness threshold only applies to point sources: we may well be missing significant numbers of extended sources that should have been selected above our flux limit. We return to a discussion of this below (Section 3.4).

The DR2 catalogue of H23 lists 1776 977 sources with `Total_flux` greater than or equal to 1.1 mJy, of which 966 323 (54.4 per cent) have an optical ID and a redshift estimate either from spectroscopy or from a good photometric redshift[2] (i.e. the `z_best` column is not blank). We further impose a redshift cut $z > 0.01$, which ensures that host galaxies are not completely resolved by the *WISE* photometry that we will use in subsequent analysis, and exclude objects that do not have any *WISE* information (including upper limits) in the *WISE* 1, 2, or 3 bands. *WISE* magnitudes in band 3 in our catalogue come from Neo*WISE* by way of the DESI Legacy Survey catalogue (Duncan 2022) and so both this and the requirement of a photometric redshift means that we require a Legacy survey detection for a source to be selected. Hereafter this flux-complete catalogue of 963 764 radio sources with redshift information, corresponding to the ‘FCOZ’ sample of H19, is referred to as the ‘parent catalogue’ or ‘parent sample’. We take the sky area covered by this the catalogue to be 5200 deg^2, based on the area of the full-band Legacy Survey coverage which is needed for photometric redshifts.

2.2 Merger with emission-line catalogue

The parent catalogue is then merged with the emission-line catalogue from D24, with duplicate columns stripped out. D24’s catalogue is based on the H23 catalogue and so can be matched exactly by LoTSS source identifier. This gives probabilistic emission-line classifications for 154 044 sources, of which 110 638 are in the parent catalogue; the remainder are below the flux density or redshift limits that we use here.

D24 provide probabilistic classifications for all objects. In particular, they give an estimate of the probability that an object is a star-forming galaxy or a radio-excess AGN based on its position in a Baldwin–Philips–Terlevich (BPT) diagram (Baldwin, Phillips & Terlevich 1981), and its measured Hα and radio luminosities. In what follows we use a 0.95 threshold on this probability calculated by D24 to select high-confidence radio-excess and star-forming galaxies (hereafter RXG and SFG) to help us to define selection regions for these classes of objects where spectroscopic data are lacking. The intersection of the D24 catalogue with the parent catalogue lists 28 065 RXG and 27 127 SFG at this confidence level.

2.3 Merger with the SDSS DR16 quasar catalogue

We finally merge the parent catalogue with the SDSS DR16 (‘quasar-only’) quasar catalogue (Lyke et al. 2020) with a simple optical positional cross-match with offset < 1 arcsec. Objects that have a match in the DR16 catalogue are very likely to be quasars; however, the converse is not true since not all quasars will have been observed spectroscopically, and in addition there is a part of the DR2 sky area that is not covered by SDSS. Moreover, the eBOSS survey, which adds significantly to the total number of high-z quasars, does not uniformly cover the SDSS footprint (Dawson

[2] As described by H23, photometric redshifts are said to be good if the `flag_qual` column of Duncan (2022) is set to 1, i.e. the photometry is free from blending and artefacts, the object is not star-like in optical images, and $\sigma_z/(1+z) < 0.2$.

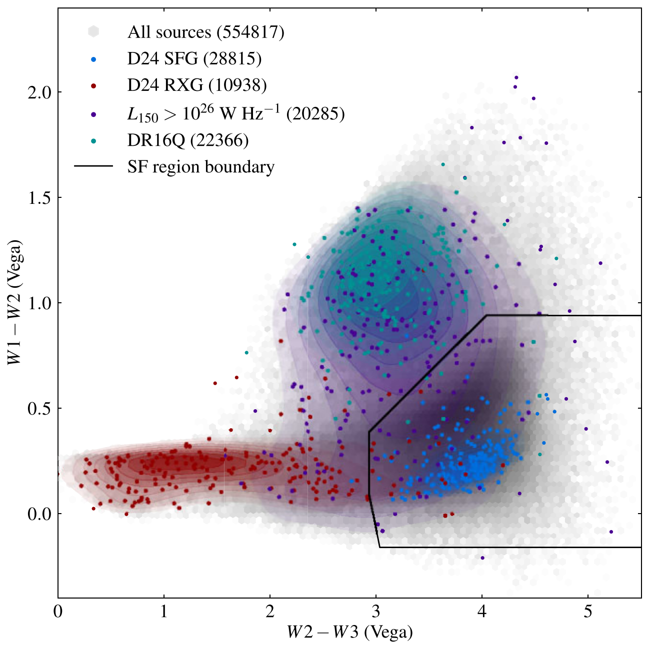

Figure 1. The observational *WISE* colour–colour diagram for the DR2 sample. Overlaid on the grey density plot showing the full parent sample with detections in all three *WISE* bands are the locations of D24 RXGs, D24 SFGs, DR16 quasars and luminous radio sources. To allow visualization of the areas occupied by each population, these are plotted as contours from the KDE estimate of the source density for the different classes, with colour contours representing intervals in source density on a square root scale. Overplotted are a small number of representative points from each subsample to give a sense of the scatter: the total number of points in the subsamples is indicated in the legend. Lines indicate the locus populated by SFG and avoided by many RLAGN discussed in the text.

et al. 2016). There are 26 567 matches to DR16 quasars in the table.

2.4 The *WISE* colour–colour plot

The selections from these two catalogues can then be overplotted on the *WISE* colour–colour plot from H23 (Fig. 1). This shows clearly that the D24 classifications correspond, like those of Sabater et al. (2019), to largely distinct regions in colour–colour space, as expected (although the D24 analysis made no use of the *WISE* colours). The approximate (hand-drawn) locus that could be used to exclude objects with SFG colours in the manner described by H19 is shown as a solid line on this plot. Also shown are the luminous ($L_{144} > 10^{26}$ W Hz^{-1}) sources, which are likely to be AGN in all circumstances, since this value exceeds any plausible level of emission from star formation: as in H19, luminous sources occupy largely distinct locations in colour space, with many lying in the region where we expect to find quasars, and the addition of the DR16 quasars confirms this.

An important point here is that we exclude from the plot objects that are not detected in any of the *WISE* bands. In practice, this mostly excludes objects without a detection in *WISE* band 3 (i.e. the error `magerr_w3` in the catalogue is not listed). Only 555 200 objects in the parent catalogue have a *WISE* 3 detection. For the others, the *WISE* magnitude is a lower limit. This has the useful feature that selection in colour space would be conservative – if we excluded from our RLAGN sample objects that lay in the SFG colour locus, we might also exclude some true RLAGN which should actually lie to the left of their position in the plot, but we would not expect to be contaminated by objects with SFG colours. The problem is that this cut would be likely to exclude a number of true RLAGN with colours in the SFG locus as well (Gürkan, Hardcastle & Jarvis 2014), and this is clearly seen in the figure, where a number of objects with $L_{144} > 10^{26}$ W Hz^{-1} would lie in the exclusion region. Although this was the approach of H19, we prefer to take a different approach here to avoid excluding radio-excess AGN with colours in the star-forming locus. Accordingly, colour selection for SFG/AGN selection is not used in the rest of the paper.

2.5 The mid-IR/radio relation

Another way of visualizing the relationship between radio power and galaxy properties is to look at the relationship between radio luminosity and IR luminosity or absolute magnitude, as noted by e.g. Mingo et al. (2016) and H23. *WISE* magnitudes are particularly interesting here as they trace different combinations of SF-heated dust and old stellar population. We form the *WISE* absolute magnitude here by converting *WISE* magnitudes to flux density,[3] computing a power-law spectral index between the flux density values, and then K-correcting the magnitudes based on this power-law extrapolation (e.g. for the *WISE* band 2 mag the spectral index between bands 1 and 2 is used). This naive approach has the advantage that it can be used without relying on templates, as the tabulated absolute magnitude values in the catalogue do; however, it clearly breaks down even in principle for $z > 0.35$ for bands 1 and 2 and $z > 1.6$ for bands 2 and 3, after which we would be extrapolating rather than interpolating between the two values. In addition, only about half the sample has a secure detection in band 3.

Nevertheless, it is instructive to look at the positions of the D24 SFG and RXG samples on this plot (Fig. 2), as they show strikingly different behaviour in the two *WISE* bands. In $W2$, we see that the SFGs trace a linear correlation which merges seamlessly into a vertical stripe for the RXGs. This is because $W2$ is simply a proxy of mass for these objects (which can be verified by plotting it against the stellar mass estimates provided by H23) and we are seeing the well-known effect that RLAGN appear in large numbers above some stellar mass threshold, corresponding to around $\log_{10}(M_*/\mathrm{M}_\odot) \approx 10.7$. However, in the $W3$ plot there is an almost complete separation between the D24 RXG and SFG. Here, it is important to bear in mind that the fact that the RXGs are mostly non-detections in $W3$ would only increase the real separation. The $W3$ band (observer-frame broad-band 7–17 μm) is dominated by hot dust from star formation and so the strong correlation between $W3$ luminosity and Hα emission means that the D24 RXG and SFG, which are by construction well separated on a plot of $L(\mathrm{H}\alpha)$ versus L_{144}, are well separated here as well. Moreover, the main-sequence line defined by the SFGs clearly continues beyond the low-luminosity SFGs from D24 (which run out around 10^{24} W Hz^{-1} or star formation rates $\sim 100\,\mathrm{M}_\odot\,\mathrm{yr}^{-1}$). We conclude that we can conservatively separate RXGs and SFGs in the $W3/L_{144}$ plot with a simple linear dividing line which, unlike the approach of H19, does not exclude objects that have SFG colours but a strong radio excess over what is expected from star formation. This approach mirrors that of Mingo et al. (2016), but we have the advantage of being able to calibrate the line independently using the D24 spectroscopic classifications. Our chosen line could exclude true RXG that have weak radio emission but strong radiative AGN-related

[3] See https://wise2.ipac.caltech.edu/docs/release/allsky/expsup/sec4_4h.html.

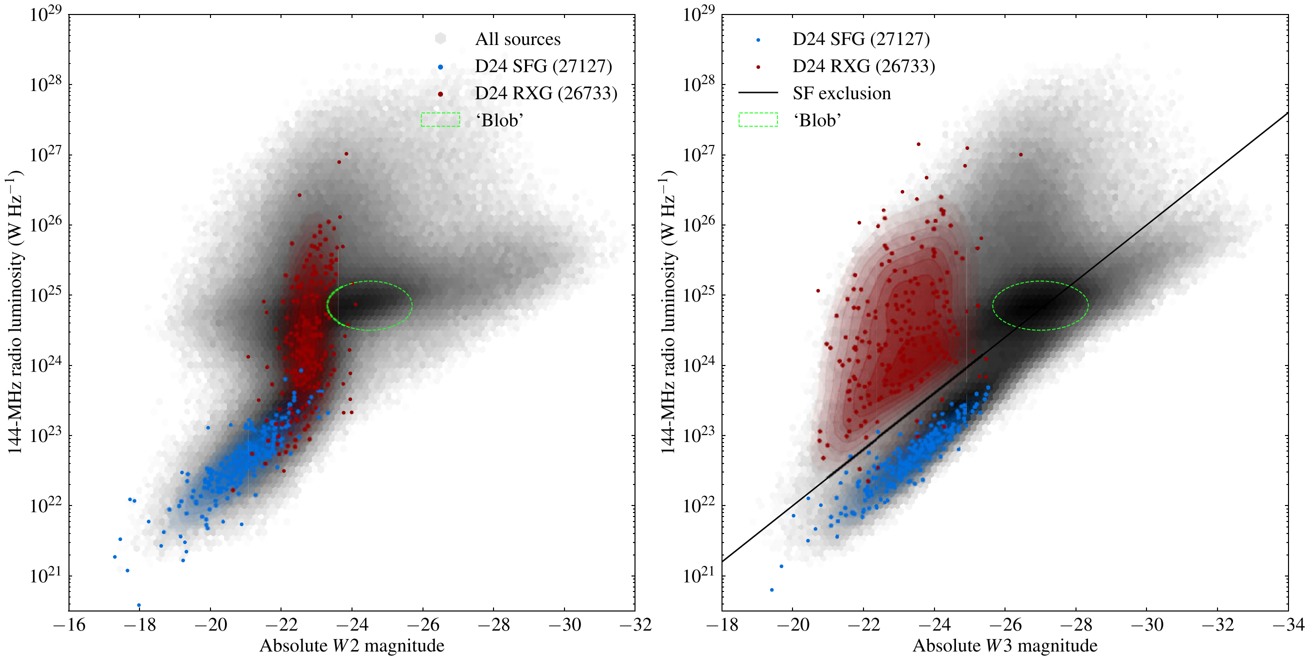

Figure 2. The absolute magnitude/radio luminosity relation for the parent sample and the two emission-line classified samples from D24. Left panel shows $W2$ magnitude and right panel $W3$ magnitude. Note that in the right-hand panel a significant number of upper limits (407 657/963 754) are plotted as though they were detections. The solid line in the right-hand panel ($\log_{10}(L_{144}/\mathrm{WHz}^{-1}) = 14 - M_{W3}/2.5$) indicates a possible dividing line below which objects can be rejected as being SFG, while the dashed ellipse shows the location of the 'blob' of objects at high *WISE* luminosities and $L_{144} \approx 10^{25}$ W Hz^{-1}. Colour contours are as in Fig. 1.

(torus) emission in the *WISE* band, but if such objects exist, they are not present in any significant numbers in the D24 sample.

2.6 Quasars

The appearance of Fig. 2 is complicated by the existence of a quasar population which gives rise to $W2$ absolute magnitudes brighter than -24 and also to bright $W3$ magnitudes, though in this case not necessarily brighter than the maximal $W3$ magnitude for a starburst galaxy, which might be -29 or so for a radio luminosity of 10^{25} W Hz^{-1}. This population will consist of both traditional type 1 quasars and also radio-loud type 2 quasars, or narrow-line radio galaxies (NLRG), since both can have excess emission over the expectation from starlight at $W2$ and $W3$ (see e.g. Hickox et al. 2017). $W3$ excess is likely to be more reliable as an indicator of RE AGN activity in general if SFG are excluded, since $W2$ is more affected by obscuration. By construction, all these objects are radio-detected, and they have radio luminosities significantly larger than the typical SFG, but they would be traditionally described either as 'radio-quiet' (RQQ) or 'radio-loud' (RLQ) based on the ratio of their radio to optical or IR luminosity.

In H19, we excluded on a similar plot (based on the Ks band at 2.2 μm) a branch of what we took to be radio-quiet quasars, which can be seen in both panels of Fig. 2 extending to the right at L_{144} values of a few $\times 10^{25}$ W Hz^{-1}. The naive star-formation exclusion line in Fig. 2, right panel, goes straight through the bulk of this population, and in particular bisects a 'blob' of objects with $L_{144} \approx 10^{25}$ W Hz^{-1} and $-25 \lesssim W3 \lesssim -27$. A similar group of objects is at $-24 \lesssim W2 \lesssim -26$.

The nature of the radio emission from RQQ is not well understood but it remains possible that some or all of it is from strong star formation (Gürkan et al. 2019): in that case one approach would just be to apply the naive line to the quasar population as well. However, that neglects the fact that the quasar must contribute to the emission in W3, and it now seems plausible that, although some quasars may be radio-silent (Radcliffe et al. 2021), the radio emission in radio-detected quasars is at least partly AGN-related (Calistro Rivera et al. 2024; Yue et al. 2024; Njeri et al. 2025). If we wished to reproduce the H19 analysis, we could cut out the 'quasar branch' seen in the plots more completely by modifying the selection line to exclude the branch and the 'blob' at its base at the cost of introducing significant (and physically unmotivated) structure into the luminosity distribution of the sample.

However, SDSS (type 1) quasars do not seem to be the dominant population of objects in the 'blob'. In Fig. 3, we show the positions on the *WISE*/LOFAR luminosity plot of D24 LERGs and HERGs together with the positions of objects identified as SDSS quasars. The SDSS quasars turn out to avoid the 'blob' region; many of these objects seem actually to be galaxies or non-SDSS quasars in the $1 \lesssim z \lesssim 2$ redshift range with $W3$ non-detections. Some may of course be quasars or extreme star-forming objects (e.g. ultra-luminous infra-red galaxies or ULIRGs at high z), but in general this part of parameter space cannot be excluded. DR16Q objects are almost all detected in W3.

2.7 Selection of RLAGN

From the preceding two subsections, conservatively we can cut out clear SFGs, and thus restrict the sample to objects where the radio emission is presumptively due to RLAGN activity, by taking objects that

(i) are detected in $W3$;

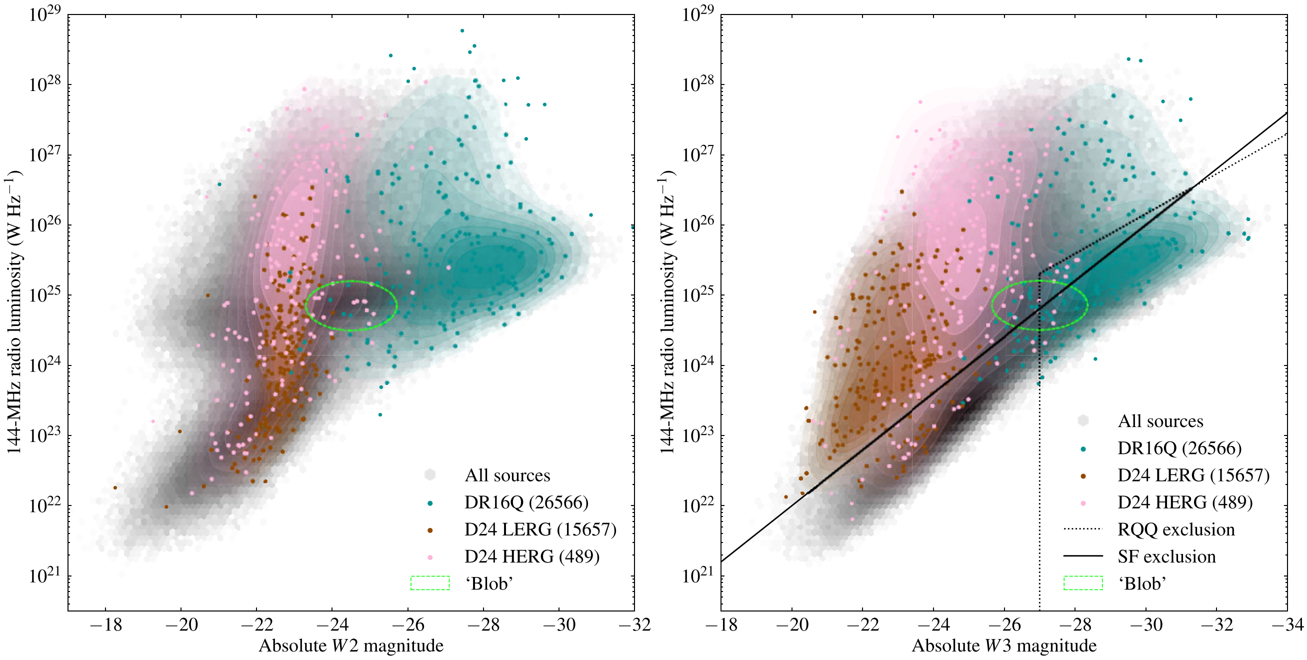

Figure 3. As Fig. 2, but with emission-line classes for RLAGN and DR16 quasars labelled. Note that there are many fewer HERGs than the other types of object plotted here: the coloured density plots represent the locations where they are most likely to be found rather than the total numbers of objects.

(ii) lie below and to the right of the SF exclusion line on the right-hand panel of Fig. 3;
(iii) have $\log_{10}(L_{144}/\mathrm{WHz}^{-1}) < 24.8$ (above which the SFG population merges into the 'blob' discussed above and then the RQQs).

This cut removes 331 221 objects whose radio emission is plausibly due to star formation from the parent sample, leaving only objects where the radio emission is above the SF exclusion line. We cannot exclude the possibility that we are excluding some objects in this way which should be included in the AGN selection (e.g. objects where the radio emission is faint but on scales much larger than the host galaxy and so cannot be due to star formation), but this is unavoidable in a simple radio excess selection and in general we lack the resolution to investigate this distinction for our parent sample.

If we wish to remove the apparent 'RQQ' branch, we can make further cuts to remove sources that

(i) are detected in $W3$;
(ii) lie below and to the right of the RQQ exclusion line on the right-hand panel of Fig. 3;
(iii) have $W3$ brighter than -27.

This would exclude a further 66 718 objects. Whether this is the correct thing to do depends partly on the science case of interest, and partly on the nature of radio emission from the 'RQQ' population (e.g. Panessa et al. 2019). In what follows, we exclude these objects for consistency with H19, and because they are generally treated separately in other analyses (e.g Mingo et al. 2016); see further discussion in Section 4.2.

This approach errs on the side of inclusivity for the RLAGN sample that remains after these cuts are made since we consider only objects detected in W3, which, as discussed above, is only a fraction of our sample, though most known SFGs from the D24 analysis and most DR16Q are detected in W3. We could err in the direction of having a cleaner (though less complete) RLAGN-only sample by also excluding objects that meet these criteria with an upper limit in W3. A comparison of the two approaches is shown in Table 1. In what follows we use the inclusive sample of 565 821 objects for further analysis.

Table 1. Results of inclusive and exclusive RLAGN selection as described in the text.

Name	Inclusive	Exclusive
Original sample	963 764	–
Star formation exclusion	331 225	357 424
RQQ exclusion	66 718	130 844
Remaining AGN	565 821	475 496

Our sample selection leads to a sky surface density of candidate RLAGN (above our completeness flux density limit) of $\sim 110\ \mathrm{deg}^{-2}$, exceeding the sky densities often estimated for IR selection (e.g. Stern et al. 2012) and notably around twice the sky density of the DR1 sample from H19. Given that we require an optical ID and a redshift, it seems very likely that this sky density is a very conservative lower limit even for sources that would meet our selection criteria. We comment further on this in Section 4.1.

2.8 Selection of radiatively efficient and inefficient objects

In the absence of emission-line classification, which will be provided for many of these objects by the WEAVE-LOFAR survey (Smith et al. 2016), detailed broad-band SED fitting is expected to be the best way of establishing the presence or absence of an energetically significant radiatively efficient (RE) AGN (e.g. Best et al. 2023; Das et al. 2024). Our data are not good enough to do this: in particular, they lack far-IR measurements that help to tie down the contribution of star formation to dust heating.

There are some alternative routes to an approximate classification, however. In the $W2$/radio luminosity relation of Fig. 3, the quasars lie generally to the luminous side of $W2 \approx -24$, while there is very little

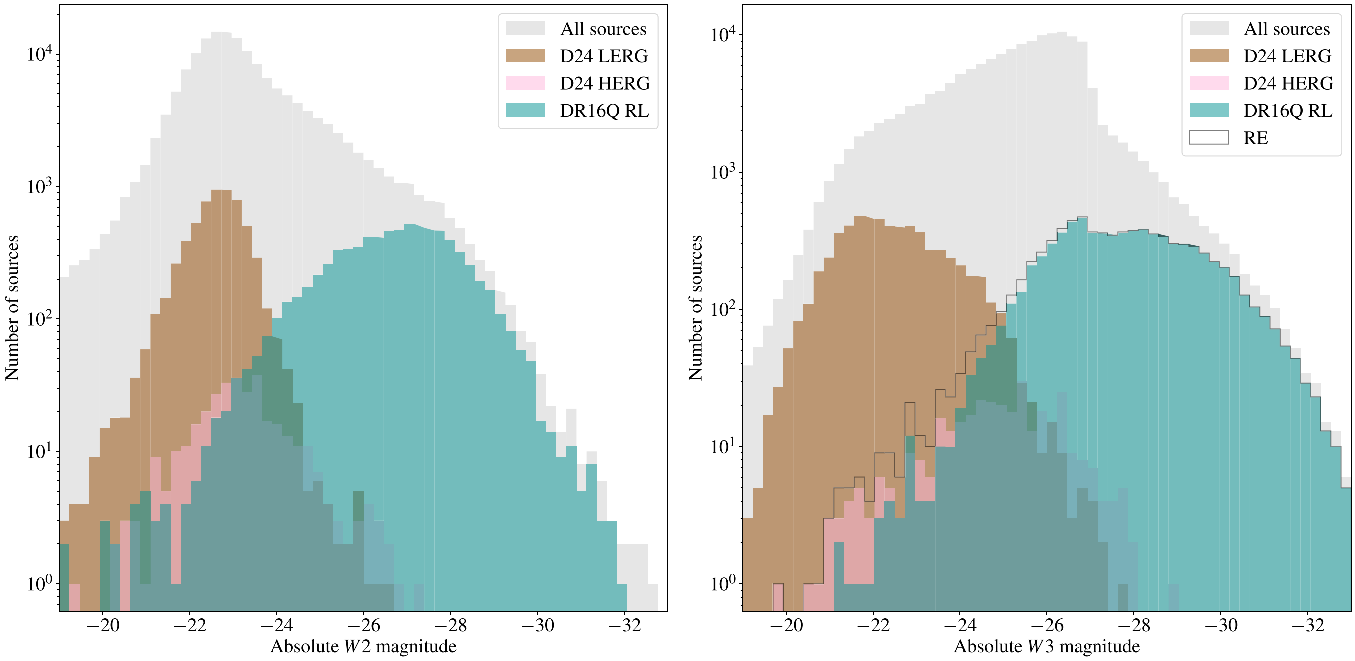

Figure 4. *WISE* magnitude distribution for RLAGN detected in $W3$ together with the distributions of emission-line classified sources. Left: $W2$ distribution. Right: $W3$ distribution, with combined D24 HERGs and DR16 quasars indicated with the RE line.

difference between D24 HERGs and LERGs[4] in this quantity (which for normal galaxies is just driven by the old stellar population); HERGs lie at typically higher radio luminosities than LERGs, with a good deal of scatter, as is well known. But in the relation with $W3$ there is a clear offset between the typical LERG and HERG locations in the *WISE* magnitude, with both D24 HERGs and DR16 quasars being to the luminous side of the distribution. Histograms of the *WISE* absolute magnitudes for the RLAGN sample of the previous section confirm this basic picture (Fig. 4). We could attempt to use cuts in $W2$ and $W3$ (requiring detections in both bands) to select and classify radiative AGN, corresponding to the suggestion of Gürkan et al. (2014), but there remains significant overlap between the HERG and LERG populations in these plots.

Alternatively, we can look at colour–colour plots (Fig. 5). Once SFG are removed, D24 LERGs (non-quasar) HERGs and DR16 quasars do sit in reasonably distinct locations on these plots, as has been seen in earlier studies (Gürkan et al. 2014; Prescott et al. 2018). Again, the problem is that there is no sharp boundary between the LERG and HERG populations in $W2$–$W3$, and that a $W3$ detection is needed for the use of any line in that colour space. Selecting a cut around $W2 - W3 > 2$ would minimize the cross-contamination between RE and RI objects for our sample but it would clearly still exist. We can also note that there is a reasonably sharp cut-off for $W1 - W2 > 0.4$ above which few LERGs exist. Taking cuts in colour space where RE objects have $W1 - W2 > 0.4$ or $W2 - W3 > 2$ (requiring a $W3$ detection for the latter) and quasars have $W1 - W2 > 0.75$ (corresponding to standard 'AGN' selection criteria, e.g. Stern et al. 2012) leads to classifying 305 078 objects as RE (of which 108 580 would be quasars and 196 498 would be non-quasar RE objects, i.e. NLRG), 57 232 as RI and 203 511 as unclassifiable (because they have $W1 - W2 < 0.4$ and an upper limit on $W2 - W3$ which does not allow them to be placed on either side of the $W2 - W3 = 2$ boundary line). It is important to note that there will be substantial cross-contamination with this method across the boundaries of the RE/RI sample (12 per cent of D24 LERGs are classified as RE by this method, for example) and also the calibration we use is best at low z, whereas we know that the positions of particular types of source on these plots are likely to evolve with z (Assef et al. 2013). Reliable and complete classification of the sample will have to await more spectroscopic information from WEAVE-LOFAR and DESI and/or better broad-band optical SEDs from *Euclid*. We will, however, use these colour-colour classifications later in the paper, while bearing in mind the substantial caveats on their application.

3 PROPERTIES OF THE CATALOGUED SOURCES

In the preceding section, we described the process of generating a RLAGN catalogue. The catalogue is released with this paper[5] and a description of the columns it contains is given in Appendix A. In this section, we carry out some checks on the properties of the catalogued objects to establish their consistency with expectations from earlier work.

3.1 Comparison with H19

The H19 catalogue made from LoTSS DR1 data cannot be compared directly with the current one because H19 used a lower (and somewhat optimistic) completeness threshold of 0.5 mJy because

[4]D24 required the emission lines needed for a BPT diagram to classify an object spectroscopically, and so were only able to classify LERGs that had these emission lines, while many absorption-line-only systems would also normally be classified as LERGs. For simplicity we refer to the 'LINELERG' class of D24 as LERGs, while noting that there will be other objects in the population studied by D24 that would typically be classified in that way.

[5]https://lofar-surveys.org/dr2_release.html

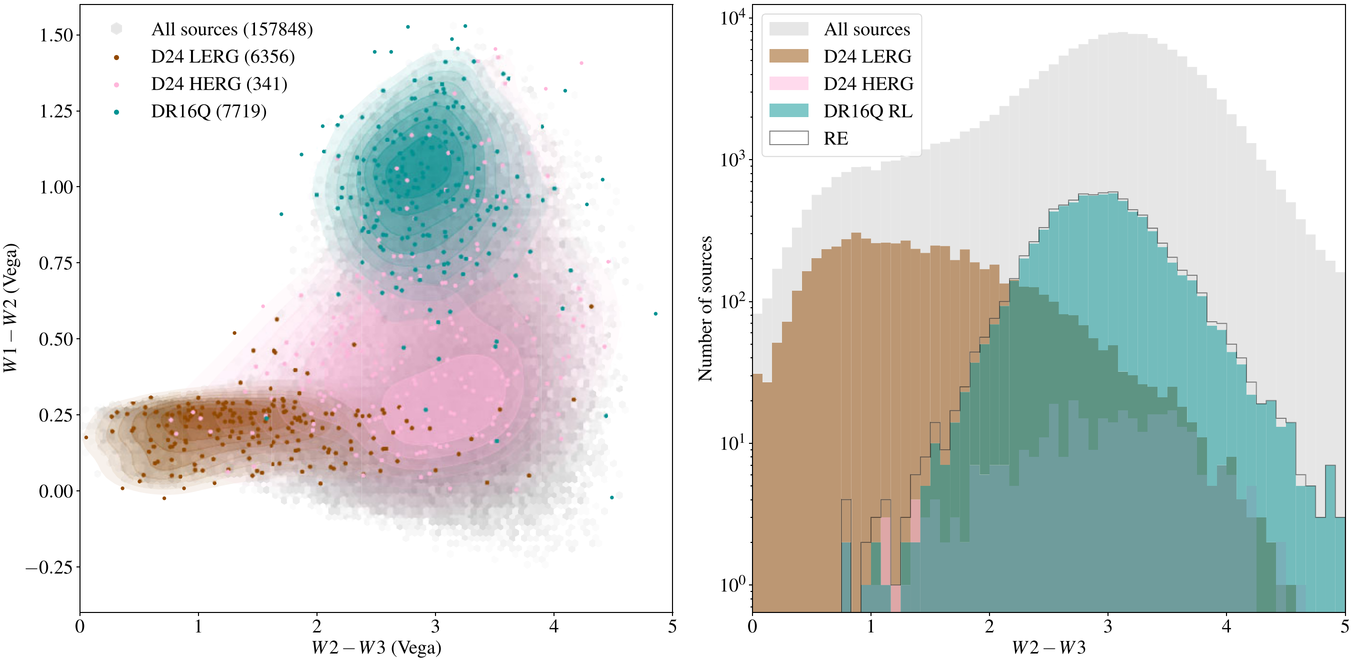

Figure 5. Left: *WISE* colour–colour plot and (right) histogram of the $W2-W3$ colour for the RLAGN sample, with emission-line classes from D24 and the DR16 quasars indicated. Note the removal of the previously dominant population in the SFG locus by the RLAGN selection, as expected. Only 157 848 sources with $W3$ detections are plotted.

of the position of their sources at the location of best sensitivity for LOFAR on the sky. However, if we cut the H19 RLAGN catalogue of 23 244 objects at our current completeness threshold of 1.1 mJy, we get 14 379 objects, of which 12 114 (84 per cent) have a matching ID position in the new parent catalogue – a match rate comparable to what we reported for the catalogues as a whole in H23. Of these 12 114, 10 979 (91 per cent) would also be classed as RLAGN in the new catalogue, with almost all the remainder being excluded as SFG: these would be objects whose location on the *WISE* colour–colour plot used by H19 is not consistent with star formation, but which lie close to the $W3$–L_{144} relation we use here. On the other hand, 1461 (10 per cent) of the objects excluded by H19 as SFG on the basis of their *WISE* colours would be classed by us as RLAGN, which is as expected given the discussion of colour selection above. We can conclude that the H19 selection is broadly picking out the same classes of object as we do here, with some scatter across the AGN/SFG boundary as expected.

3.2 Source counts

Extragalactic radio source counts are expected to be dominated at the bright end by RLAGN and at the faint end by star-forming galaxies and RQQ, and as a sanity check we present the source counts broken down by classification in Fig. 6. No completeness correction is carried out, since we believe that the lower flux cut of our parent sample ensures good completeness. The expected picture is seen, with SFG dominating the numbers of sources only at the very lowest flux density levels. RQQ do not dominate at any flux density in these classifications but are most important at flux densities of a few mJy. These results are very consistent with those of, e.g. Hardcastle et al. (2016) or Siewert et al. (2020), with the only clear difference being the significantly better statistics in the present work, and qualitatively in agreement with models such as those of Wilman et al. (2008), although there are differences in detail (see Siewert et al. 2020 or Mandal et al. 2021 for a more detailed discussion). We note that we may be incomplete to SFGs at the bright end of the number counts because of the lower redshift cut imposed as part of our selection, and of course we are still only able to classify the 58 per cent of the sample that have optical IDs and redshift information. Source counts for the LoTSS deep fields DR1 field ELAIS-N1 (Sabater et al. 2021) are also plotted, broken down according to the SED-fitting classifications of Best et al. (2023), and these show encouragingly consistent results with our much simpler classification scheme, with the exception that almost all the unclassified sources in DR2 (those that do not meet our ID and redshift selection criteria) are classified as AGN in the deep fields. We return to this point in Section 4.1.

3.3 Distributions of key quantities

Fig. 7 shows the distribution of luminosity, size, redshift, and stellar mass for the RLAGN, SFG, and RQQ samples. These show the expected separation between the two sets of quantities, although a small number of SFG with physical size $>$ 100 kpc is unexpected and may indicate from contamination of the SFG sample by RLAGN, or, perhaps more likely, poorly measured physical sizes for SFG which may be represented by large Gaussians in PyBDSF fitting. Of note is the steep decline of RLAGN above $z\sim 1.2$ – massive galaxies are no longer detected by the Legacy survey above this redshift. SFG cannot have $\log_{10}(L_{144}/\mathrm{WHz}^{-1}) > 24.8$ in our separation scheme and so a sharp feature appears in their luminosity distribution as well, but otherwise the luminosity and redshift distributions are not too different to those of our earlier work with different AGN/SF separation methods (Hardcastle et al. 2016; H19): the main difference is that we are sensitive to sources at higher redshifts and so have more RLAGN overall and in particular more luminous RLAGN than in the previous work. The stellar mass distribution shows strong overlap between the SFG and RLAGN hosts, as expected from e.g. Fig. 2, but a clear tendency for RLAGN hosts to be more massive overall.

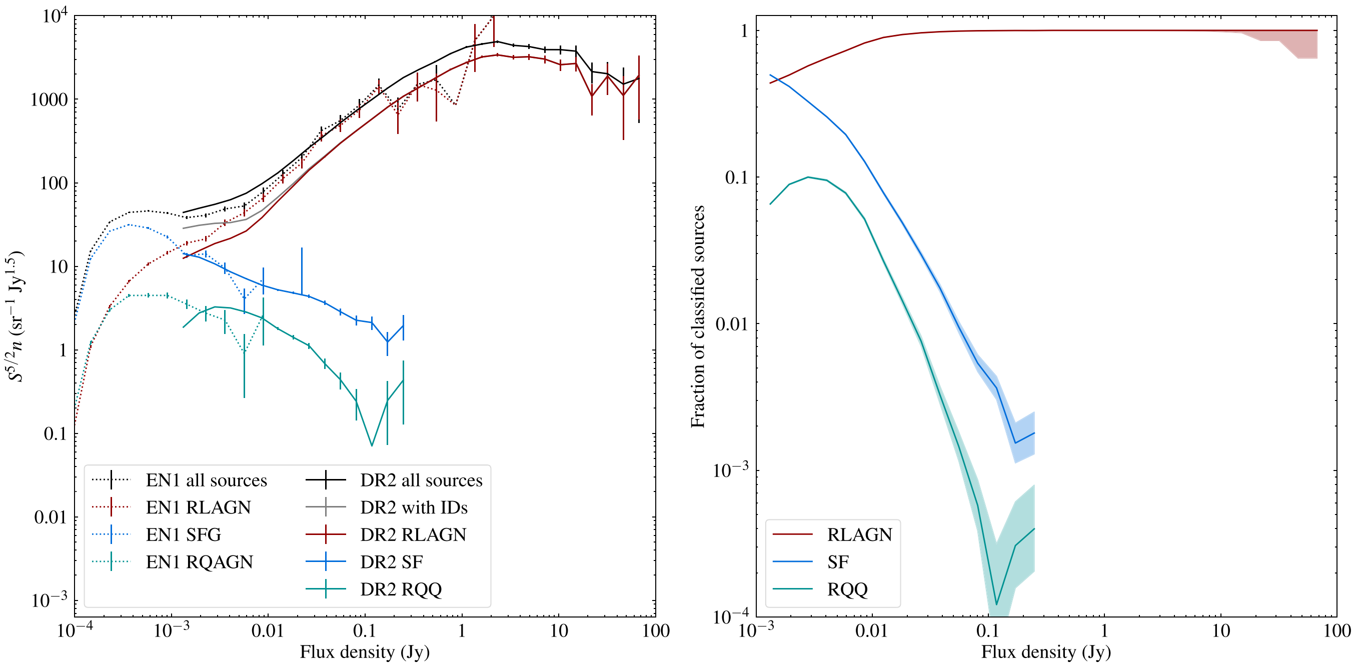

Figure 6. Left: Conventional Euclidean-normalized differential source counts as a function of flux density for the overall LoTSS catalogue (after component association through visual inspection) above the flux density limit, the full parent catalogue, and the sources classified as RLAGN, SFGs and RQQ, together with the ELAIS-N1 source counts classified by Best et al. (2023) which are shown as dashed lines. Error bars are Poissonian. The ELAIS-N1 counts are not corrected for incompleteness at the faint end. Right: The fraction of the parent catalogue classified as RLAGN, SFG, or RQQ as a function of flux density, with Jeffreys interval binomial uncertainties plotted as the shaded area.

We miss low-mass SFGs in general because they will not be detected in the radio other than at very low redshift, thus biasing the SFG mass distribution high. As noted by H23, not all galaxies in the sample have reliable mass estimates, and of course no quasars do: overall 73 per cent of RLAGN and 80 per cent of SFG are plotted here.

3.4 Power-linear size diagram

Fig. 8 shows the power-linear size (P–D) diagram for the RLAGN sample. Relative to the similar figure shown by H19, this plot contains far more sources and probes deeper into the low-surface-brightness regime to the right hand side of the plot due to the improved sensitivity of LoTSS DR2. Individual sources' evolution causes them to describe tracks in this plane: representing the whole population on such a plot gives us a sense of the range of properties that objects in the sample have, particularly when combined with theoretical models. As the plot shows, if we (unsafely) ignore the wide range of environments and redshifts that are represented within the sample, the objects that we select span seven orders of magnitude in kinetic power and have maximum ages ranging from 10^7 yr to several Gyr. Due to the size of the sample and the sensitivity of LoTSS DR2, we select an unprecedentedly large number of physically very large sources, as reported by Mostert et al. (2024), and we can see that these must probe the extreme high-age end of the visible source lifetime distribution.

What is also apparent from this figure is two key limitations of our selection that will affect future analysis using the sample. The first is the large number of unresolved sources. Only 118 498 objects in the sample (21 per cent) have reliable size measurements. As shown by Sweijen et al. (submitted), a much larger fraction of sources have size measurements when 6-arcsec images made using the Dutch LOFAR baselines are combined with the full 0.3 arcsec available using the International LOFAR Telescope, but we are still some way away from having these high-resolution images for wide sky areas like those of LoTSS DR2. Size information for a sample provides key information about the age distribution, as discussed by H19, and in particular could help us to determine the distribution of lengths of accretion event that drive jet activity (the lifetime function). A multimodal lifetime function would be implied, for example, by the idea that a substantial fraction of young radio sources selected as Compact Symmetric Objects (CSOs) are actually triggered by tidal disruption events (TDEs) as proposed by Readhead et al. (2024). Accurate size measurements of a large sample like the present one, selected in as unbiased a way as possible directly from low-frequency surveys, are crucial to making these inferences across the population. These will be available in the future through processing of the long-baseline LoTSS data and through the proposed ILoTSS project.[6] Since the constraints on the lifetime function from the existing data have an influence on the inference of radio AGN feedback effects, we will discuss them in more detail in a future paper (Pierce et al. in preparation).

The second limitation of our selection is the surface brightness limit, which manifests itself as a sharp cut-off in the sampling of P–D space below and to the right of the diagonal line in Fig. 8. Physically large sources can be detected but only if they are also luminous: we have no way of knowing whether there are, say, Mpc-scale RLAGN with $L_{144} = 10^{23}$ W Hz^{-1}, since they are simply undetected in our sample. More subtly, some large objects will be detected in the LoTSS images but will not be included in our selection because it has not been possible to identify them optically;

[6] https://lofar-surveys.org/ilotss.html

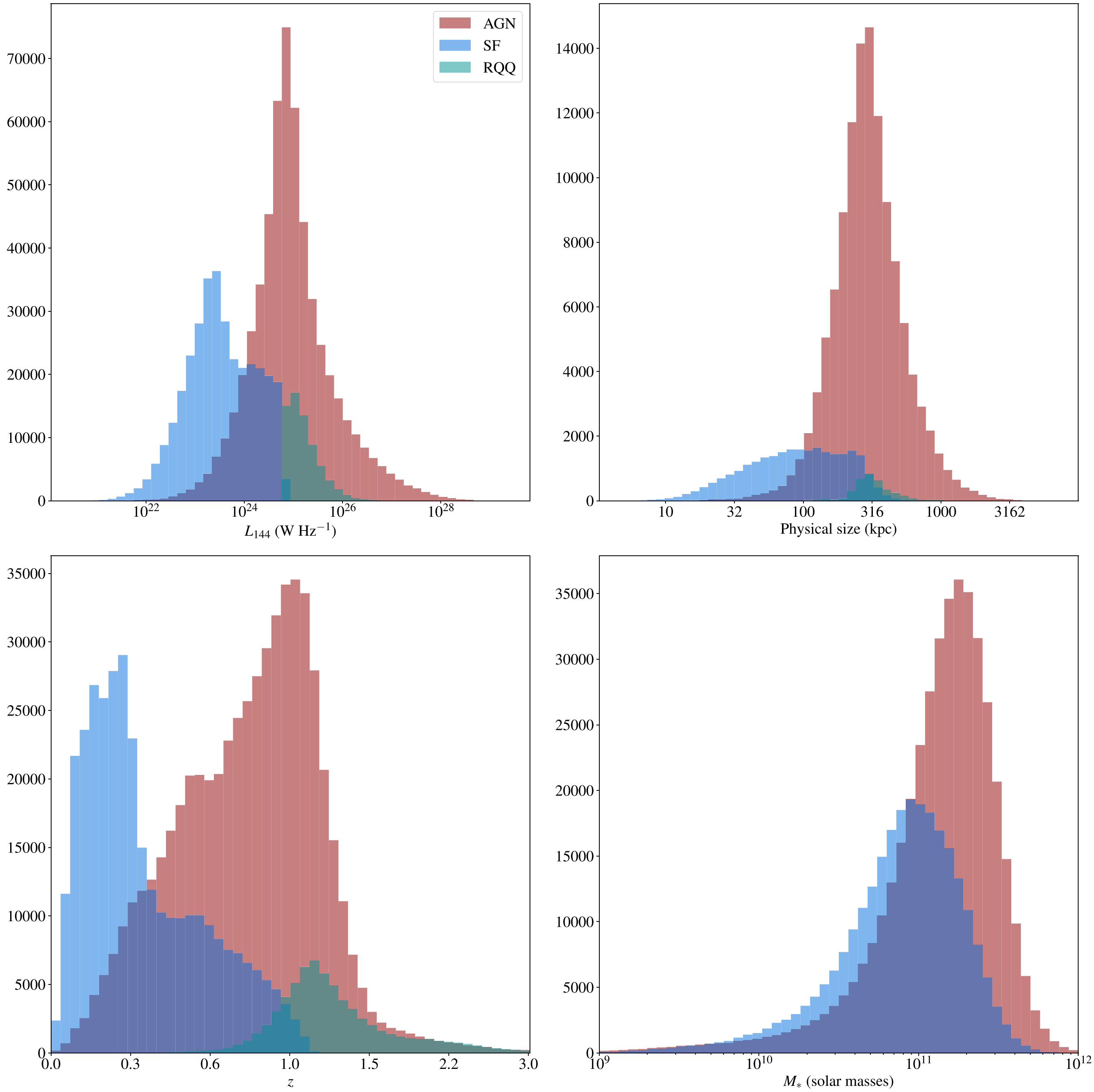

Figure 7. Luminosity (top left), size (top right), redshift (bottom left), and host galaxy stellar mass (bottom right) distributions of the three catalogues. In the size histogram, only resolved sources as defined by H23 are plotted, while the RQQ sample is excluded from the mass histogram and only objects with `flag_mass= = True` are shown.

for example, remnant sources with no compact structure may be particularly difficult to associate with a particular host galaxy (e.g. Brienza et al. 2017). Oei et al. (2023) and Mostert et al. (2024) have shown that dedicated methods of searching for diffuse sources and/or of their optical identifications can increase the numbers of detections, but these methods only somewhat shift the boundaries of the area of the P–D plane that we are not sensitive to rather than removing it altogether. Analysis of the size (and therefore, as discussed, age/lifetime) distribution of RLAGN, or of the populations of special types of RLAGN such as remnant sources, needs to take account of this effect since even next-generation surveys will not fully remove the bias for the faintest objects. We estimate that in the current sample only the most luminous sources ($> 10^{26}$ W Hz^{-1}) are unaffected by surface brightness limits, and even here the completeness is likely to be reduced by the challenges of optically identifying all of these physically large sources.

With these caveats, the population of the P–D plot and the comparison with models still gives some insights into RLAGN physics. For example, there is a region in the top right of the plot (powerful, physically large sources with nominal jet powers $10^{39} < Q < 10^{40}$ W) which is almost completely unpopulated, although these objects would be easily detected if they existed. This tells us that the most

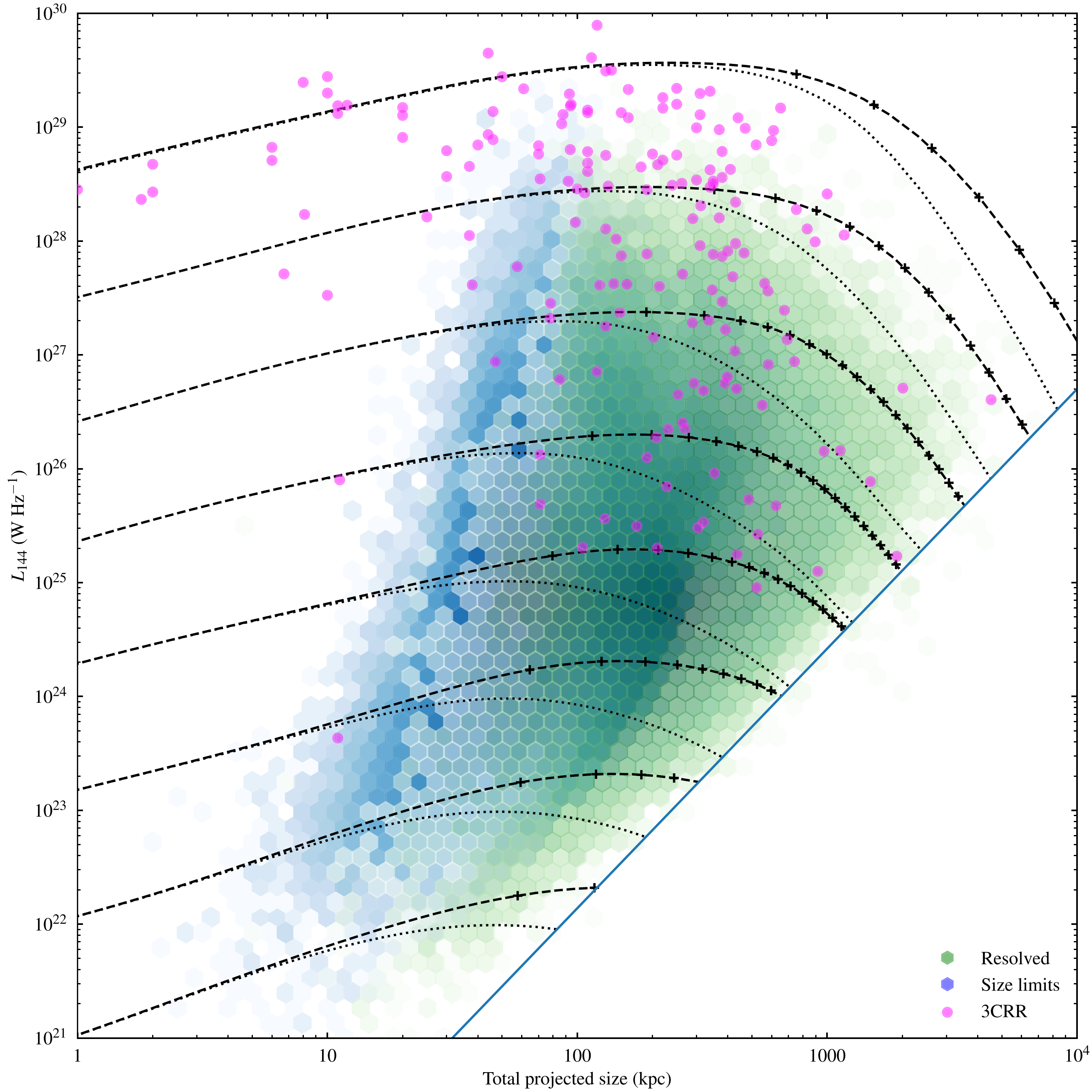

Figure 8. Power/linear size plot for the RLAGN sample. All 565 821 RLAGN are plotted: the green density plot indicates size estimates for sources that are resolved by LOFAR as defined by H23 while the blue points are for sources that are unresolved, in which case the size should be taken as an upper limit. We also show the positions of 3CRR sources (Laing et al. 1983) for comparison. A solid blue line indicates the approximate region that cannot be populated due to the surface brightness limit of LoTSS. We overplot $z = 0$ (dashed) and $z = 1$ (dotted) theoretical evolutionary tracks in this space (Hardcastle 2018b) for sources lying in the plane of the sky in a group environment ($M_{500} = 2.5 \times 10^{13}$ M$_\odot$, $kT = 1$ keV) for two-sided jet powers (from bottom to top) $Q = 10^{33}, 10^{34}, \ldots, 10^{40}$ W (see the text for details). Crosses on the $z = 0$ tracks are plotted at intervals of 50 Myr, with linear size increasing monotonically with time.

powerful jets, whose powers are of the order of the Eddington luminosity for a 10^9 solar mass black hole, almost never live beyond ~ 100 Myr. Less powerful sources, with $10^{38} < Q < 10^{39}$, clearly can persist for much longer and (because of the surface brightness selection effect) most of our extreme giant sources are in this category (cf. Oei et al. 2024).

3.5 Colour–colour classification compared with other methods

Since our colour–colour classification of RLAGN will be used later in the paper we here compare its results briefly with that from other work. Fig. 9(a) shows a comparison with the 3CRR catalogue (Laing et al. 1983) which has complete spectroscopic classifications for

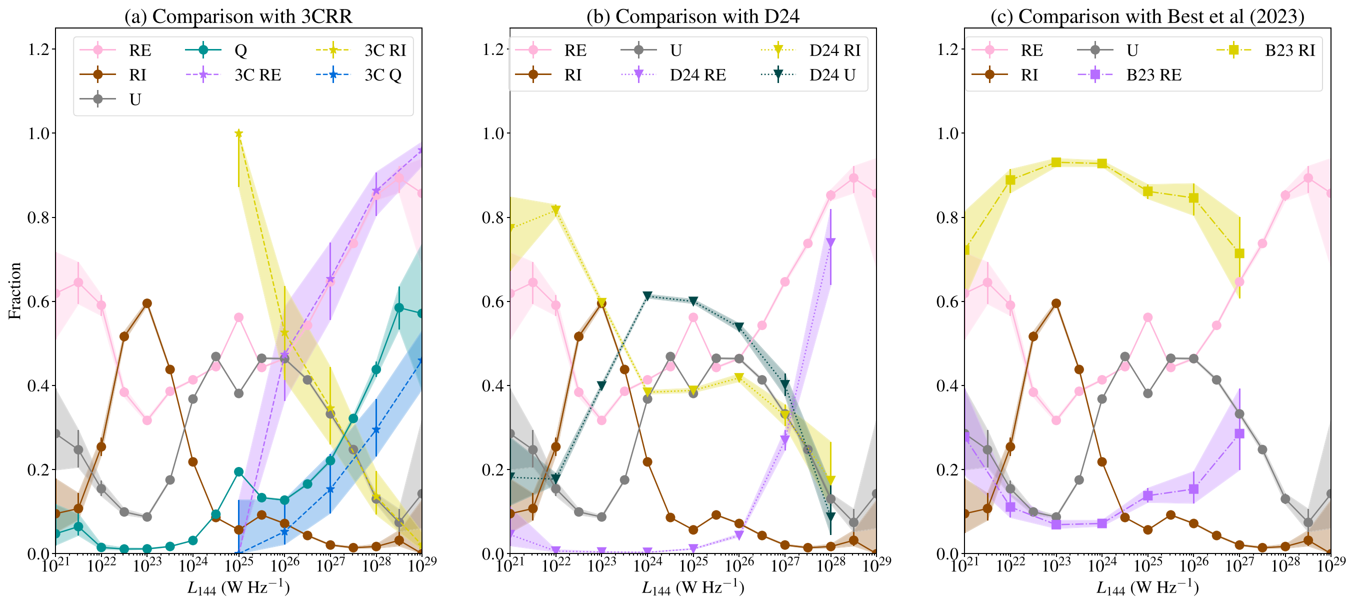

Figure 9. A comparison of the *WISE* colour–colour plot classifications with those from other work. All panels show the proportion of objects with particular classifications as a function of the total RLAGN at a given L_{144} with $z < 1.2$. From left to right, we compare our classifications with (a) the 3CRR catalogue, (b) D24, and (c) Best et al. (2023). Shaded regions show the binomial credible intervals. For clarity, luminosity bins where there would be fewer than four sources in total are not plotted.

luminous sources. The agreement here is remarkably good, including with the proportion of quasars, if we assume that almost all our unclassified objects are RI at $L_{144} > 10^{26}$ W Hz^{-1}. The proportion of RE objects that we obtain is much higher at the lowest luminosities, though. Panel (b) compares with D24 and we see that again the agreement is reasonably good at high luminosities, particularly as some of D24's unclassified objects will certainly be RE. However, at low luminosities, we obtain many more RE objects and we suggest that this is likely due to contamination of our sample by lower mass galaxies that are intrinsically RI but have star-forming colours, or of course by some objects that should have been excluded as SFGs but are not removed by our selection criterion. This is particularly clear around 10^{25} W Hz^{-1} as there is a localized peak in RE objects that must be related to the SFG maximum luminosity at $\log_{10}(L_{144}/\mathrm{WHz}^{-1}) = 24.8$. Finally, the comparison with Best et al. (2023, hereafter B23) shows strong disagreement at all luminosities, with B23 having a much higher proportion of RI objects throughout; however, this means that B23 also strongly disagree at moderate to high luminosity with the spectroscopic classifications of 3CRR and D24, which is surprising. If we ignore the discrepancy with B23, we can conclude that our classification should give consistent results with previous *spectroscopic* classification at $L_{144} > 10^{26}$ W Hz^{-1}, with the unclassified objects at high luminosity plausibly being mostly RI.

4 DISCUSSION

4.1 How many radio AGNs are there?

We noted above (Section 2.7) that our RLAGN selection gives a sky density of ~ 100 deg^{-2}. We know on the basis of the source counts (Section 3.2) that there must be a large number of additional RLAGN in the parent sample not identified as such by us: at a minimum, all of the sources with flux density larger than a few mJy that do not have an optical counterpart and a secure redshift seem likely to be RLAGN with a high-z host galaxy. Given that the redshift fraction in the sample stands at 58 per cent at the moment, it is plausible that the true sky density of RLAGN with flux density > 1.1 mJy is a factor 1/0.58 $= 1.7$ times larger than our estimate. Indeed, the catalogues and SED-based classification of Best et al. (2023), using the LoTSS deep fields where the optical identifications are almost complete, give a sky density of 160 deg^{-2} RLAGN above our flux cut in the ELAIS-N1 field, consistent with this estimate, and this can be seen in the source counts plot of Fig. 6, where the RLAGN line for ELAIS-N1 lies consistently above ours in the range where they overlap. While the detailed classification of sources through SED fitting and spectroscopy may change, the number count arguments imply that this conclusion is likely to be robust.

We can also see from the number counts that a substantial number of radio-excess RLAGN are likely to exist at flux densities below our cut of 1.1 mJy. As noted above, the optical data become insensitive to massive galaxies above $z \approx 1.2$, at which point, by chance, an $\alpha = 0.7$ radio source with $S_{144} = 1.1$ mJy has a luminosity almost exactly at our adopted cut-off for star formation, around 7×10^{24} W Hz^{-1}. Thus, not only are we insensitive to high-z AGN because of our optical data, but also as we move to high z our flux density cut prevents us from including in our sample objects that would be unambiguously AGN by our selection criteria even if their host galaxies were detected (see further discussion of this in the following subsection). Again, the Best et al. (2023) catalogue can be used to get a sense of the order of magnitude of this effect: in ELAIS-N1 there are 670 deg^{-2} objects classed as radio-excess AGN in total, so that the objects that are below our completeness flux cut actually dominate numerically over these that are above it. As the deep-fields catalogue samples down to the point where SFG start to dominate the number counts of radio sources, a number of the order of 1000 deg^{-2} is likely to be an upper limit on the sky density of true radio-excess AGN (taking account also of the effects imposed by surface brightness limits as discussed in Section 3.4). Hence, we can conclude that we have found around a tenth of all of the RLAGN by this definition in the DR2 sky area. Even so, the sky densities of RLAGN even in our current wide-area survey are already comparable with those of optically selected AGN expected from next-generation wide-area surveys such as *Euclid* (Euclid Collaboration et al. 2025), consistent with the result of Sabater et al. (2019) that all massive galaxies have AGN-related radio emission at some level. Deeper wide-area radio sky surveys such as the proposed ILoTSS survey, which will cover a similar sky area to LoTSS DR2 but at twice the depth and 0.3 arcsec resolution, or deep and wide surveys with the forthcoming SKA, should be expected to select all the radio-excess AGN in their sky coverage.

We finally return to a point made in Section 1.1: even if it can be done with complete accuracy, *radio-excess* selection does not in practice capture all sources that have non-negligible radio emission due to AGN activity. Many star-forming galaxies, including arguably the Milky Way, show radio emission that is the result of past or present activity of the central supermassive black hole but that does not currently dominate over the radio emission due to star formation. A complete census of the black-hole activity in the Universe would need to account for these low-level but potentially very numerous sources with both star-formation and AGN-related radio emission, and doing so would almost certainly give a significantly larger radio AGN sky density (Morabito et al. 2025).

4.2 The nature of the RLAGN population

As noted in Section 1.1, there are in principle a number of different mechanisms that can produce AGN-related radio emission, not limited to the powerful jets that dominate the high-luminosity radio AGN population (Hardcastle & Croston 2020). Since we select as an RLAGN any source whose radio emission exceeds the prediction from the mid-IR/radio relation (Section 2.5) we are potentially including different physical types of object in our sample. Panessa et al. (2019) list some of the different mechanisms for generation of radio emission from what they describe as 'radio-quiet' AGN, but it is important to understand that an object that is 'radio-quiet' by their definition – which can only consistently be applied to radiatively efficient classical AGN, since it relies on optical or X-ray emission from the accretion disc – could also be 'radio-luminous' by ours. Thus, our sample could be 'contaminated' by objects whose radio emission in excess of star formation is generated by e.g. disc winds or coronal emission rather than by a jet. If the RQQ are removed as discussed above (Section 2.7), then such objects in our sample would be limited to objects that do not lie in the RQQ exclusion region (Fig. 3), perhaps including some of the 'blob' population discussed in Section 2.6. We expect this population to be most important at low radio luminosities, and there is considerable evidence for a group of low-luminosity compact RLAGN in the LOFAR population (H19) including some that are clearly radiatively efficient AGN (Chilufya et al. 2024). At present there is no way of separating these objects out of our sample (or any other) in the absence of detailed information about the radiative AGN contribution to our sample from spectroscopy, and so their presence in the sample should be borne in mind in what follows.

4.3 The evolution of the RLAGN luminosity function

The wide-area LOFAR observations give us an unrivalled view of the rare, luminous RLAGN in the universe out to the point where we start to run out of optical identifications at $z \approx 1$. One way of parametrizing this population and its cosmological evolution is to construct the radio luminosity function as a function of redshift (e.g.

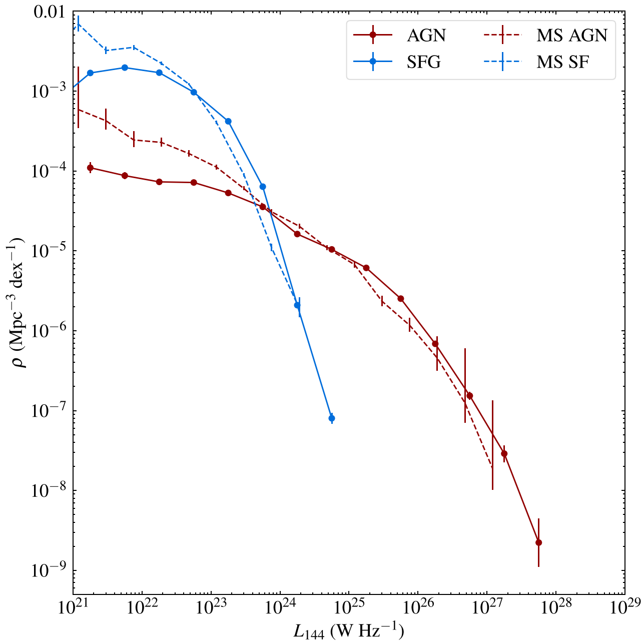

Figure 10. The luminosity function of LOFAR sources (left) in the range $0.01 < z < 0.3$, with both RLAGN and SFGs shown and the results of MS07 plotted for comparison.

Condon 1984; Dunlop & Peacock 1990; Willott et al. 2001; Mauch & Sadler 2007; Prescott et al. 2016; Smolčić et al. 2017; Novak et al. 2018; Williams et al. 2018; Kondapally et al. 2022; Wang et al. 2024) and in this section we use our RLAGN/SFG separation to investigate the cosmological evolution of the overall RLAGN population. The very large number of objects in the sample means that we can get a much more precise view of the evolution of the luminosity function, particularly at the high-luminosity end, than has previously been possible.

Luminosity functions are constructed following the standard $\rho = \sum_i 1/V_i$ method (as described by Schmidt 1968; Condon 1989), where $V_i = V_{\rm max} - V_{\rm min}$ is the volume within which a given radio galaxy could have been observed with the available observations and sample criteria (following Williams et al. 2018). $V_{\rm min}$ is the volume enclosed within the observed sky area out to the minimum distance at which a target could have been observed, derived from the minimum redshift limit in the given bin. $V_{\rm max}$ is the volume enclosed out to the maximum available distance for the target, considering the imposed *WISE* Band 1 flux limit ($W1 < 21.2$ mag) and the upper redshift limit for the bin: we discuss the details of the optical $V_{\rm max}$ calculation in Appendix B. Error bars are Poissonian.

Fig. 10 shows the overall luminosity function for the RLAGN in the sample for $z < 0.3$, along with the local luminosity function of Mauch & Sadler (2007, hereafter MS07), for comparison, converted to 144 MHz assuming $\alpha = 0.7$. Unsurprisingly, our LF is in reasonable agreement with that of MS07, but we have significantly fewer objects at the lowest luminosities, which we attribute to missing optical IDs differentially at the low-flux end (H23). We know from the work of e.g. Kondapally et al. (2022) that the local LF from the LoTSS deep fields, with essentially complete optical IDs, is more in line with the MS07 results – our results are more in line with the wide-field work of Sabater et al. (2019). The lowest-luminosity bins are populated by relatively low numbers of objects, so small changes in the optical ID fraction can make a large difference. We may also be classifying slightly more objects as SFG than MS07 did

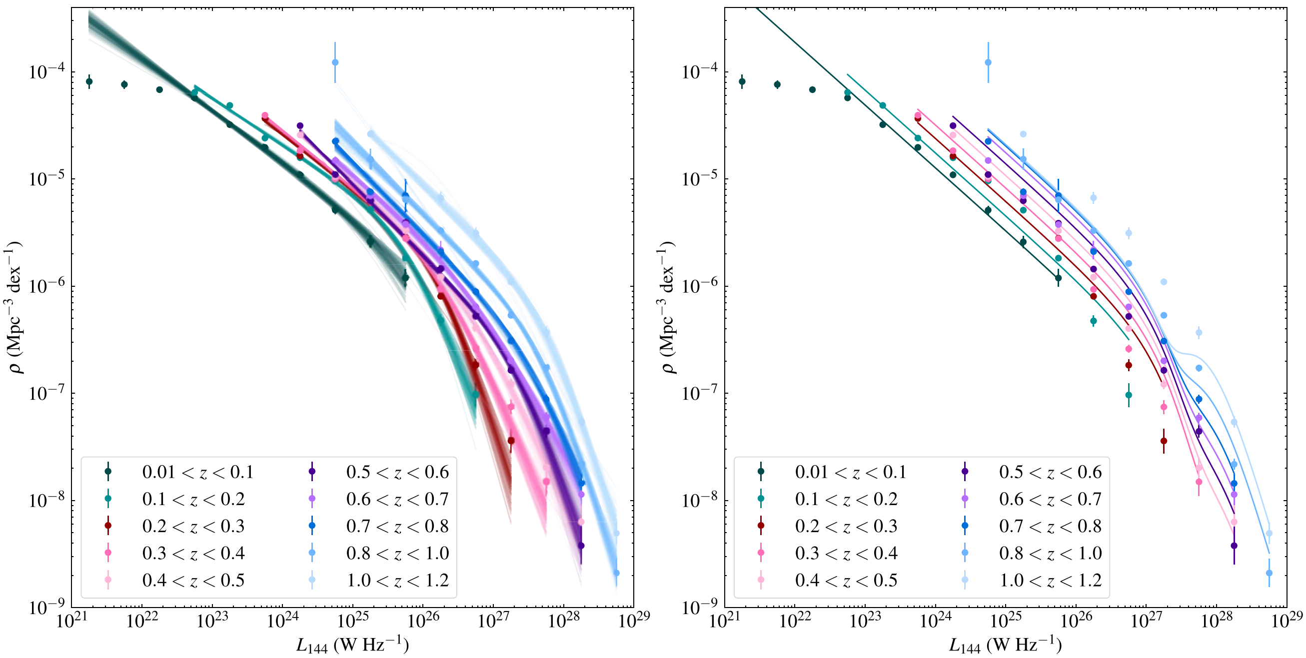

Figure 11. The luminosity function of LOFAR RLAGN as a function of redshift. Colours show different redshift bins: points with error bars are the measured values. Left: The lines show samples from the MCMC inference of the parameters of a dual power-law model. Right: The lines show the predictions of the models of Willott et al. (2001) converted to the cosmology and luminosity units of this paper.

in the luminosity range 10^{23} to 10^{24} W Hz^{-1}, but a direct comparison is hard given that the SFG population shows strong cosmological evolution.

More interesting is the redshift evolution of the whole RLAGN population, seen in Fig. 11. As we have such large numbers of sources, we can construct precise luminosity functions in very small redshift bins compared to previous studies, and hence can carry out a much more model-independent analysis of the cosmic evolution of the population than is generally the case in earlier studies. We binned the RLAGN sample in redshift out to $z = 1.2$ in steps of $\Delta z = 0.1$ out to $z = 0.8$ and $\Delta z = 0.2$ thereafter, reflecting the increased uncertainties on the photometric redshifts at the high-z end. We then fitted each luminosity function with the dual power-law model used by Dunlop & Peacock (1990) and MS07,

$$\rho(L) = \frac{C}{(L/L_*)^{\alpha} + (L/L_*)^{\beta}}, \tag{1}$$

where C gives the normalization of the luminosity function at $L \approx L_*$, L_* is the characteristic break luminosity and α and β are the power-law indices at low and high luminosity, respectively. We used the EMCEE sampler (Foreman-Mackey et al. 2013) to carry out a Markov chain Monte Carlo (MCMC) fit to the data above $L_{144} = 3 \times 10^{22}$ W Hz^{-1} for each redshift bin with a χ^2 likelihood function, leaving all four parameters free: C and L_* have uninformative uniform priors in log space, while we require $0 < \alpha < 1$ and $1 < \beta < 2.5$ to ensure that the power-law parameters are not degenerate. Credible intervals on the fitted parameters, and their best value estimates, were then derived from the (16, 50, 84)th percentiles of samples on the marginalized distribution for each parameter. 100 random samples from the `emcee` run (after the burn-in samples where the MCMC code has not yet converged are discarded) are overplotted on the data in Fig. 11, where it can clearly be seen that the higher redshift bins have systematically higher luminosity cut-offs and higher normalization.

The evolution of the population is made quantitative in Fig. 12 where we plot the parameters of the fit as a function of redshift: as L_* and C are correlated, we illustrate the evolution of normalization by plotting ρ_{25}, the comoving source density at a fixed luminosity of 10^{25} W Hz^{-1}, inferred from the model fits. It can be seen that the inferred L_* increases by nearly three orders of magnitude over the redshift range sampled here. It is hard to see how redshift/optical ID incompleteness could bias this evolution of L_* in this positive direction, and, viewed as pure luminosity evolution, it is very strong ($\log(L_{*,\mathrm{max}}/L_{*,\mathrm{min}})/\log(1 + z_{\mathrm{max}}) \approx 8$ out to $z = 1$). Although it is possible that there is contamination from luminous SFGs that are not excluded from our RLAGN selection because they fall above the luminosity limit, we do not expect them or contaminating 'radio-quiet AGN' to be important at the very high break luminosities seen at high z. ρ_{25} also evolves positively with redshift.

A useful comparison is with the models of Willott et al. (2001), who use a two-population model for low-luminosity and high-luminosity RLAGN (intended to represent RI and RE objects in our terminology, respectively). Taking their model C and converting to our cosmology, we find reasonable agreement with the data at low z, as shown in Fig. 11, but relative to us they overpredict the density evolution of low-luminosity objects at low z and underpredict it at the highest z, while coming close to the observed evolution of high-luminosity objects.[7] This is perhaps not surprising as low-luminosity objects at high z would have been poorly constrained by the data they used, which had a much higher flux density limit.

More recent work (Smolčić et al. 2017; Wang et al. 2024) has used deep fields to study cosmological evolution of the low-luminosity population out to high redshift. Relative to our work, these studies generally have smaller numbers of AGN sources and do not probe

[7]The slight kink in the predicted LF at high luminosity and redshift is a consequence of the two-population model used by Willott et al. (2001) and is present in the original paper.

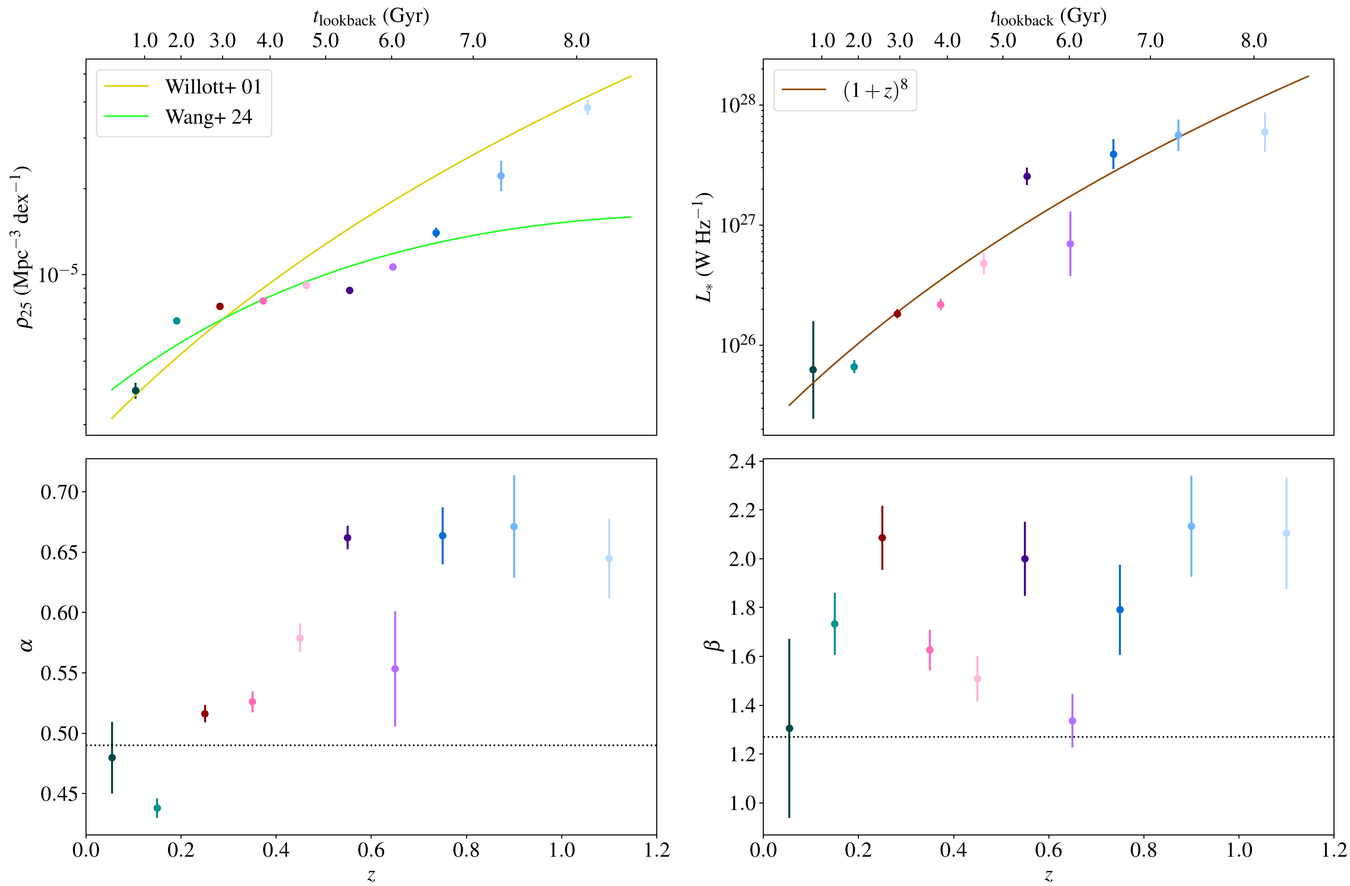

Figure 12. Evolution of the fitted parameters of a dual power-law model as a function of redshift. Top left: ρ_{25}, the normalization of the luminosity function at 10^{25} W Hz^{-1}, with overlaid curve of $(1 + z)^{3.48}$ as expected from the models of Willott et al. (2001), together with the fitted pure density evolution model of Wang et al. (2024), both normalized to align with the data. Top right: the characteristic turnover luminosity of the dual power-law luminosity function, L_*, with overlaid curve of $(1 + z)^8$ to show the strong redshift dependence of this parameter. Bottom left and right: the parameters of the two power laws α and β respectively, where the dotted lines show the MS07 values of these parameters. The x-axes show redshift and lookback time (light travel time). Colours of the points are as in Fig. 11. Error bars show the one-dimensional 68 per cent confidence credible intervals on the derived parameters, and thus do not account for correlations between parameters.

the most luminous objects. There is therefore a degeneracy between density and luminosity evolution in these samples that is not present in our work, where the wide area ensures that we have a wide range of radio luminosities for every redshift bin. On the other hand, the deeper optical and radio data available for deep fields means that they can probe to considerably higher redshift than is possible for us. To limit the numbers of degrees of freedom, deep field studies have tended to fix the parameters of equation (1) to those determined in the local universe, e.g. by MS07, giving a local luminosity function $\rho_0(L)$, and then fit for luminosity or density evolution of the form:

$$\rho(z, L) = (1 + z)^{\alpha_D} \rho_0 \left(\frac{L}{(1 + z)^{\alpha_L}} \right), \tag{2}$$

where α_D and α_L parametrize the density and luminosity evolution, respectively, and can be constants or functions of z. A key difference between these analyses and ours is that our fits are strongly inconsistent with constant values for the parameters α and β in equation 1, while they agree with MS07 at $z = 0$. Indeed, the evolution of our break luminosity (Fig. 12) is largely driven by the apparent steepening in α with redshift, though there is some positive evolution even if we fix α to its local value. The evolution of number density at fixed luminosity is relatively independent of these choices, though, and as seen in Fig. 12, we are in reasonable agreement with the parametrization of Wang et al. (2024) out to $z \approx 0.8$, but then infer stronger evolution of the AGN number density than they do, more in line with that of Willott et al. (2001). This difference is even stronger if we force the parameters L_*, α and β to have their local values. Given the relatively coarse redshift binning necessarily used in the deep-field work, it seems possible that the discrepancy may indicate a more complex evolution of the RLAGN population, with a less smooth dependence on cosmic time, than is visible in small-sample studies.

We can also compare with the work of Kondapally et al. (2022) using the LoTSS deep fields, who find only modest positive luminosity evolution and negative density evolution in what they class as the LERG population in bins of $0.5 < z < 1.0$ and $1.0 < z < 1.5$ – at the highest redshifts it seems possible that the discrepancy between this and our results is due to the higher fraction in our sample of rare but luminous HERGs, which have been found to evolve strongly in earlier studies (Best et al. 2014; Pracy et al. 2016). Again, detailed comparison with earlier work that looks at the HERG/LERG difference will need to await spectroscopic source classifications. With deeper optical/IR data for identifications and more spectroscopic or photometric redshifts, as will be provided by *Euclid* among other facilities, it should be possible to push an

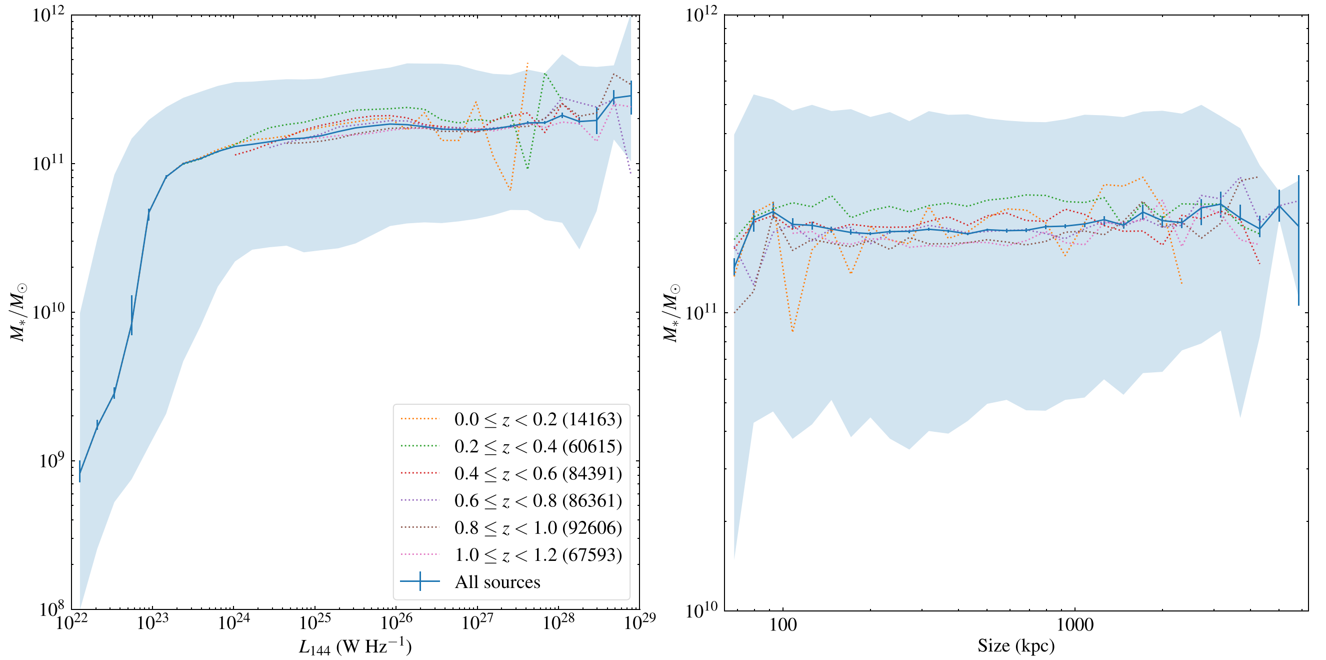

Figure 13. Host galaxy stellar mass estimates as a function of radio luminosity (left) and source linear size (right). Only sources with `flag_mass= = True` are plotted in both figures, and a redshift cut $z < 1.2$ is imposed. Both panels show binned median (logarithmic) masses together with their 1σ bootstrap uncertainty (line and error bars) together with the 5–95 percentile range of the mass estimates to give a sense of the breadth of the distribution (shaded area). Both panels also present a breakdown of the population into redshift bins (coloured lines: error bars not shown for clarity). The left-hand figure shows all 405 729 RLAGN that meet our selection criteria. In the right-hand figure only the 49 961 resolved sources with $L_{144} > 10^{25}$ W Hz^{-1} are shown. Note the different scales on the y-axes of the two plots.

analysis of this type in the wide fields, with excellent statistics, out to the point where the space density of RLAGN starts to decline again.

4.4 Host galaxy masses and radio luminosity dependence

Host galaxy stellar mass estimates[8] are available for around 73 per cent of the RLAGN sample, excluding any quasars; for the sample with $z < 1.2$ 81 per cent of sources have mass estimates that we treat as reliable, following H23. The mass estimate success rate is nearly 100 per cent for $z \lesssim 0.7$ and falls off with redshift above that, as expected as the signal to noise of the optical data deteriorates. While a more complete set of mass estimates would be ideal, the data allow us to explore the relationship between radio properties, source classification, and galaxy mass.

The left panel of Fig. 13 shows the mean mass of host galaxies as a function of radio luminosity. Our large sample gives excellent statistics, with the median being very accurately measured in spite of the large dispersion in masses for any given radio luminosity. We see that there is a very strong dependence of mean mass on luminosity for low luminosities, below $L_{144} \approx 10^{23}$ W Hz^{-1} – it is possible that this is an effect of incompleteness at the low luminosity end, since only objects above 7×10^{24} W Hz^{-1} can be seen over the full redshift range shown here. Alternatively, it may be an effect of the presence of non-jetted radio AGN in the population at low radio luminosity as discussed in Section 4.2. However, the characteristic mass flattens out above this radio luminosity, and thereafter the mean mass is between 1 and 2×10^{11} $M_\odot$ over 4–5 orders of magnitude in radio luminosity, with the scatter being broad but consistent over this range. This of course is another view of the well-known K–z relation for radio galaxies (e.g. Lilly & Longair 1984; Willott et al. 2003; Rocca-Volmerange et al. 2004) but here seen in physical terms. The trend in the median, in the sense that galaxies with $L_{144} = 10^{28}$ W Hz^{-1} are around a factor 2 more massive on average than galaxies with $L_{144} = 10^{24}$ W Hz^{-1}, is shallow but clearly significant, and is not a redshift effect since it is seen over a broad range in redshift. Host galaxies are also typically more massive, for a given luminosity, at lower redshift, but the difference here is less than a factor 2 across the entire redshift range we can sample (i.e. about half of cosmic time). It is interesting that the highest masses are seen at $0.2 < z < 0.4$ and not $z < 0.2$, but this may be a selection effect in the sense that the most massive galaxies are simply rarer in the lowest-redshift bins. The differences that we see are in line with the differences in K-band absolute magnitude seen by Willott et al. (2003), assuming that the magnitude simply scales with stellar mass, and with the results of Williams & Röttgering (2015). Considering these typical host galaxy masses to correspond to black hole masses as in the relationship derived for nearby ellipticals (Kormendy & Ho 2013) then we can say from the range of jet powers in our sample (Section 3.4) that the radio galaxy hosts in the region where the mass is independent of radio luminosity span a broad range of Eddington ratios, between $\sim 10^{-5}$ and ~ 1. We will return to this point in a future paper when individual per-source jet power estimates are available.

The right-hand panel of Fig. 13 also shows that for resolved sources there is essentially no dependence of host galaxy mass on size. Sources that have a well-measured length > 100 kpc tend to

[8]Stellar mass estimates are as described by H23 and Duncan (2022), and are based on the optical and *WISE* band 1 and 2 photometry, making use of SED fitting of a set of parametric star-formation histories derived using the Bruzual & Charlot (2003) stellar population synthesis models and a Chabrier (2003) initial mass function.

be a little more massive (a factor ~ 1.5) than the population above $L_{144} = 10^{25}$ W Hz^{-1} as a whole, but there is no evidence that the host galaxies of the extreme Mpc-scale giants are in any way different from their smaller counterparts. This is also not a redshift effect. Similar conclusions were reached on the basis of the K-band absolute magnitude distribution by H19, but our sample is much larger.

4.5 Flat-spectrum cores in extended sources

In the study of compact or flat-spectrum features of RLAGN, the VLASS survey offers important complementary information to LoTSS. To give an example of how it can be used we selected a sub-sample of the RLAGN with $L_{144} > 10^{26}$ W Hz^{-1} and with largest angular size > 60 arcsec in order to look for emission from the compact radio source coincident with the optical host galaxy, known as the radio 'core'. The luminosity cut ensures that we will mostly be looking at FRII-type objects (Fanaroff & Riley 1974) and the angular size cut leverages the fact that VLASS spatially filters structures with scale $\gtrsim 30$ arcsec, helping to reduce contamination from extended emission. The luminosity cut also puts us in the range where *WISE* colour–colour classifications appear to be most consistent with earlier spectroscopic work (Section 3.5). These two selections applied to the inclusive RLAGN sample give us 8862 objects in total.

We selected all VLASS quick-look observations available in June 2024 and initially stacked all of them around the position of the radio source to give the deepest image. The flux density of the core is then taken to be the flux density of the brightest pixel within 2 arcsec of the optical ID position, so long as it is detected at $> 5\sigma$. This gives a total of 5206 detections at 3 GHz (58percnt): the detection threshold is dependent on the field and on the number of VLASS images available, but the mean rms noise in the VLASS images is 76 μJy beam^{-1}, so that we are sensitive to core flux densities typically $\gtrsim 400$ μJy at 3 GHz. We further cross-matched the positions of the optical IDs to the LoTSS Gaussian catalogue and the FIRST catalogue, requiring a compact component (deconvolved size <6 arcsec) within 2 arcsec of the position of the optical ID. This gives respectively 2462 and 1641 core candidate detections at 144 and 1400 MHz (28 and 18 per cent). Core prominence for our sample can be defined by taking the ratio of the core flux density at a given frequency to the total flux density at 144 MHz, with the caveat that the absolute values of prominence will depend on the frequencies used. Spectral indices can be calculated for cores detected at more than one frequency, bearing in mind that of course we do not have simultaneous observations at the three frequencies so that the spectral indices will be affected by variability.

Finally, the fact that we have multiple images for essentially all of the VLASS sources (5198) allows us to compute a variability index, defined as the reduced χ^2 for a fit of the mean flux to all the individual flux measurements:

$$\chi^2_{r,VI} = \frac{1}{N-1} \sum \frac{(S_i - \mu)^2}{\sigma_i^2},$$

where $\mu = \bar{S_i}$ and we take $\sigma_i = 0.1 S_i$ to take account of the fact that the dominant uncertainty in these images is likely to be absolute flux calibration which it is reasonable to set at the 10 per cent level. Apparently, significant variability at 3 GHz is detected in a non-negligible fraction of the sources, with $\chi^2_{r,VI} > 3$ for 387 sources. Some of these are likely to be spurious due to such factors as incorrect source identification or poor fidelity in the VLASS images: we discuss the possible contamination fraction and show some images in Appendix C. However, we believe that in general we are seeing real variability in the VLASS data.

Distributions of the core prominence, variability index and spectral index are plotted in Fig. 14. There is no strong dependence of core variability or spectral properties on source luminosity or physical size, though a downward trend of core prominence with 144-MHz luminosity is observed (Fig. 15). The most striking results of this analysis come from combining it with the RLAGN classification of Section 2.8. 70 per cent of the sources with VLASS-detected cores have a classification from the *WISE* colour selection described in that section. Key points to note are as follows:

(i) Quasars have significantly more prominent, more variable and flatter-spectrum cores than the sample as a whole or than NLRG (non-quasar RE objects).

(ii) Quasar selection with the *WISE* colour–colour diagram (specifically $W1 - W2 > 0.75$) selects objects that are generally less extreme than, but similarly positioned to, the SDSS DR16 quasars. This gives some confidence that the colour-based quasar selection is working as expected, although there may be some contamination.

(iii) Radiatively inefficient objects (LERGs) have systematically low core prominence in this sample but behave similarly to NLRG in the other plots.

The absolute values on the spectral index distribution plots should be treated with caution since there are many non-detections and, as VLASS is the most sensitive of the surveys to flat-spectrum cores, the spectral indices measured here will be strongly biased towards relatively steep-spectrum cores which can be detected both by VLASS and by one of the other two surveys. Similarly, too much should not be read into the differences in spectral indices for quasars and other sources since, in the absence of a complete sample, we do not know for certain whether this is simply an effect of quasars having more prominent cores, which permits the detection of flatter-spectrum counterparts at other frequencies.[9] But the overall results for quasars and NLRG are qualitatively very consistent with the expectations from unified models, in which quasars' cores are more strongly Doppler-boosted and hence would be expected to be more prominent (Orr & Browne 1982), more variable and (assuming a downward-curved intrinsic spectrum) flatter-spectrum. Similar differences between the core prominence distributions of quasars and NLRG have of course been seen before in complete samples such as 3CRR (Hardcastle et al. 1998; Mullin et al. 2008; Marin & Antonucci 2016) but this is by far the largest sample, albeit an incomplete one, in which such an analysis has been possible. The variability effect has not previously been detected to our knowledge, although it is a straightforward expectation from the unified model, and this illustrates the value of the time-domain information provided by VLASS. Quantitative tests of unified models, and measurements of key parameters such as the effective beaming Lorentz factor as in Mullin et al. (2008), would require us to define a complete sample, ideally with spectroscopic AGN classification and also without the angular size limits imposed by our use of the VLASS data, and we hope to be in a position to carry out such a study in the coming years.

The core prominences we find are quantitatively systematically high with respect to 3CRR samples (we show the relationship between our sample and the core prominence data from Mullin et al.

[9]In order to get a sense of whether this is so for the spectral index and variability plots, we carried out the same analysis with VLASS core flux densities restricted to a narrow range between 5 and 20 mJy. The results were qualitatively very similar and a significant excess of flat-spectrum, variable quasars over NLRG was detected, which suggests that this bias is not solely responsible for the observed effect.

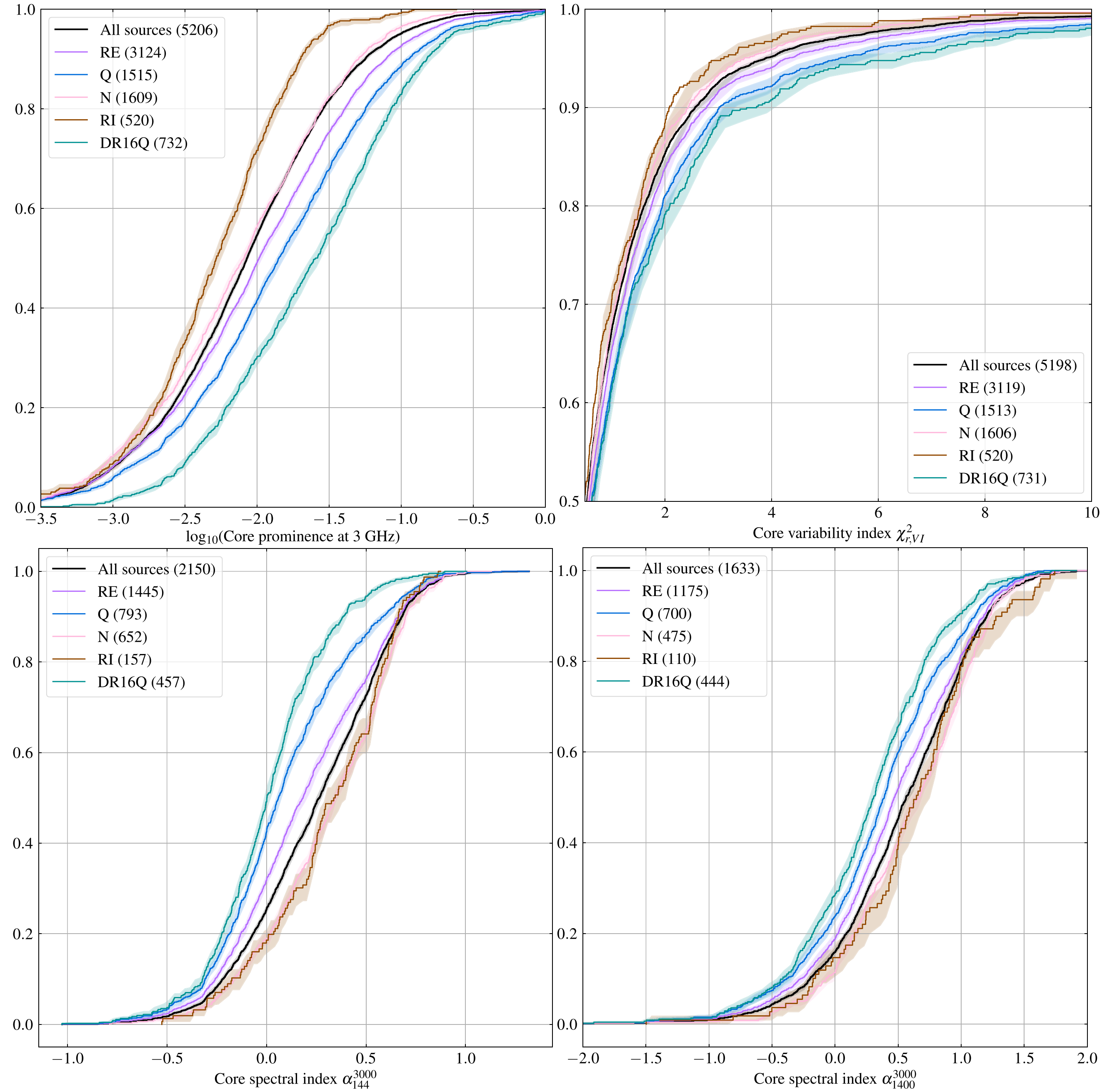

Figure 14. Cumulative distribution functions of core-related quantities separated by classification. Each line shows a CDF for a quantity (in some cases restricted to the region of interest) and colours indicate different subsamples classified from the *WISE* colour–colour diagram as described in Section 2.8. Subsamples are indicated by the abbreviations RE (radiatively efficient) and RI (radiatively inefficient, i.e. LERGs): the RE subsample is further divided using the *WISE* colour into narrow-line radio galaxies (N) and quasars (Q). SDSS DR16 quasars are also plotted; almost all of these are also in Q. For each line a region of statistical uncertainty is indicated by a shaded area indicating the 1σ range of the CDF derived from 100 bootstrapped samples from the same data set. The plots show: top left, base 10 logarithm of the core prominence, defined as the VLASS 3-GHz flux density divided by LoTSS total flux density; top right, variability index as described in the text; bottom left, core spectral index between VLASS and LoTSS; bottom right, core spectral index between VLASS and FIRST.

(2008) in Fig. 15) but this is easily understood in terms of the luminosity dependence of core prominence observed in the data, together with the fact that 3CRR objects generally have deeper observations available which can probe down to lower core prominences than we can detect for our targets. The systematically low core prominence for RI objects (LERGs) is perhaps surprising given that studies of low-z 3CRR sources have typically found similar core prominences to those of NLRG and quasars/BLRG (Hardcastle et al. 1998). In a complete sample, and with all other things being equal, we would expect RI objects to be observed to lie at all angles to the line of sight and hence to have a similar distribution to the combined RE population. Several possible explanations can be advanced. First, we can note that highly beamed LERGs will appear as blazars, and these will almost certainly be under-represented in our sample, since firstly they are unlikely to have a redshift either from spectroscopic or photometric methods, and secondly they will be impossible to classify using

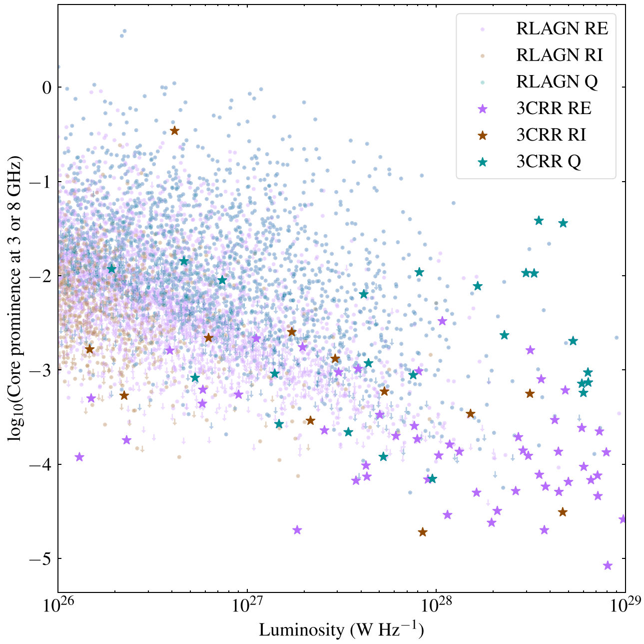

Figure 15. VLASS core prominence as a function of luminosity for the sample of large, luminous objects described in the text. 5σ upper limits are denoted with arrows. Overplotted are the core prominences (mostly at 8 GHz) tabulated for $z < 1.0$ 3CRR FRII sources by Mullin, Riley & Hardcastle (2008). A general downward trend in core prominence with luminosity is seen, with the 3CRR objects lying in a location consistent with the trend.

the colour–colour methods. By contrast, highly beamed RE objects (quasars) will if anything be over-represented in our sample with respect to their unbeamed counterparts. This, however, should only really affect a small fraction of the overall RI population. A more subtle effect is that the angular size selection we apply in order to obtain a clean core prominence estimate places constraints on source age (larger sources are in general older) and so it is possible that if LERGs in the sample have overall lower jet power, they are typically older at the point where they meet our luminosity and angular size selection criteria, and hence have lower core prominence. Testing this hypothesis would require sensitive high-resolution (sub-arcsec) radio imaging which is capable of detecting cores even in compact sources, in order to allow as complete as possible a sample to be used in these tests. We do note however that Whittam et al. (2016, 2022) found RE objects (HERGs) to have a higher rate of core detection, and therefore presumably prominence, than RI objects, albeit with a different HERG/LERG separation method than in the present paper.

Chilufya et al. (2025) present a detailed study of the properties of extended sources in the D24 catalogue, including the distribution of VLASS/LOFAR core prominences in objects classified spectroscopically as LERGs and HERGs.

5 SUMMARY AND FUTURE WORK

Using selection methods based on the optical ID catalogue for LoTSS DR2 (H23), the spectroscopic classifications of D24, and the *WISE* magnitudes for optically identified sources, we have carried out RLAGN/star formation separation and generated by far the largest catalogue of candidate radio AGN to date, with close to 600 000 objects even if the likely radio-quiet quasars are excluded. The selection is consistent with, but we believe more robust than, our earlier work on selection of RLAGN in LoTSS DR1 (H19), while providing a sample ~ 25 times larger thanks to our deeper optical data and more robust SF/AGN selection.

We are still some way from having a complete sample in which all radio sources above some flux threshold have optical IDs and redshifts, and we discuss in the paper some of the limitations of the LOFAR data, including the limited number of size measurements and the surface brightness limits that prevent us finding large, low-luminosity sources that presumably exist at some level.

Based on our catalogues and the work on the LoTSS deep fields, we have presented an empirical estimate of the total sky density of radio-excess AGN (Section 4.1). Despite the sensitivity of our survey and the high sky density of RLAGN, we estimate that we are only identifying around 10 per cent of all the radio-excess AGN in the sky with surveys at this depth (principally missing faint and/or high-redshift objects). The large number of objects in the sample allows us to model the evolution of the luminosity function in narrow bins, and we have shown that there appears to be strong positive density and luminosity evolution of the radio-excess AGN population over the cosmological time to which we are sensitive (Section 4.3). Our results are different in detail from some widely used modelling based on smaller samples (e.g. Willott et al. 2001) as well as the latest results from deep fields (e.g. Kondapally et al. 2022; Wang et al. 2024), emphasizing the value of large samples in constraining this evolution.

Bearing in mind the clear caveats about completeness of the sample, we have been able to demonstrate the value of combining the data with ancillary data either present in our existing source catalogues (e.g. the host galaxy mass estimates) or available over the same sky area (e.g. the VLASS cores), obtaining results that would be much harder to find in a smaller sample. Interesting outcomes include the identification of a weak but significant relation between radio luminosity and mean mass for luminous RLAGN, in the sense that the most powerful radio galaxies are also on average the most massive (Section 4.4), and the detection for the first time of spectral index and variability properties of the cores of resolved sources that are consistent with the prediction of unified models (Section 4.5).

LoTSS Data Release 3 (DR3), which will be the final LoTSS wide-area data release and will cover almost all of the northern extragalactic sky, is expected in 2025 and will have the potential to generate even larger samples for detailed statistical analysis, with a factor ~ 3 more sources. The proposed ILoTSS extension of the survey[10] will go significantly deeper than either DR2 or DR3 and have greatly improved capabilities for RLAGN/SF separation thanks to the long international baselines of LOFAR. The limiting factor is now, and will continue to be, the lack of wide-area optical photometric and spectroscopic data deep enough to identify all the radio sources, estimate their redshifts and carry out RLAGN/star formation separation. Additional spectroscopic redshifts and spectroscopic source classifications, coming in future from WEAVE-LOFAR and DESI, and/or the availability of deeper optical data over a wide area, such as will be provided by the *Euclid* wide-area surveys, will allow all of these conclusions to be made more robust and allow us to start to probe the full range of cosmic time over which RLAGN are active. It is our intention to release further versions of the catalogue covering the DR2 area as new data become available.

One of our key aims in generating this catalogue was to enable a statistical investigation of RLAGN feedback out to $z \approx 1$ as a function of environment and cosmic time, and this will be presented in a followup paper (Pierce et al. in preparation).

[10] https://lofar-surveys.org/ilotss.html

ACKNOWLEDGEMENTS

MJH is grateful to Ski Antonucci for discussions which motivated the work described in Section 4.5. We thank George Miley for comments on an earlier draft of the paper. We thank an anonymous referee for constructive comments which allowed us to improve the paper.

MJH and JCSP thank the UK STFC for support [ST/V000624/1, ST/Y001249/1]. KJD acknowledges support from the STFC through an Ernest Rutherford Fellowship [ST/W003120/1]. YG acknowledges PhD studentship funding from the Open University. MAH acknowledges support of STFC under a grant to the University of Cambridge [ST/Y000447/1]. BM acknowledges support from the STFC for an Ernest Rutherford Fellowship [ST/Z510257/1]. DJBS acknowledges support from the STFC [ST/V000624/1, ST/Y001028/1].

LOFAR is the Low Frequency Array, designed and constructed by ASTRON. It has observing, data processing, and data storage facilities in several countries, which are owned by various parties (each with their own funding sources), and which are collectively operated by the ILT foundation under a joint scientific policy. The ILT resources have benefited from the following recent major funding sources: CNRS-INSU, Observatoire de Paris and Université d'Orléans, France; BMBF, MIWF-NRW, MPG, Germany; Science Foundation Ireland (SFI), Department of Business, Enterprise and Innovation (DBEI), Ireland; NWO, the Netherlands; The Science and Technology Facilities Council, UK; Ministry of Science and Higher Education, Poland; The Istituto Nazionale di Astrofisica (INAF), Italy.

This research made use of the Dutch national e-infrastructure with support of the SURF Cooperative (e-infra 180169) and the LOFAR e-infra group. The Jülich LOFAR Long Term Archive and the German LOFAR network are both coordinated and operated by the Jülich Supercomputing Centre (JSC), and computing resources on the supercomputer JUWELS at JSC were provided by the Gauss Centre for Supercomputing e.V. (grant CHTB00) through the John von Neumann Institute for Computing (NIC).

This research made use of the University of Hertfordshire high-performance computing facility and the LOFAR-UK computing facility located at the University of Hertfordshire (https://uhhpc.herts.ac.uk) and supported by STFC [ST/P000096/1], and of the Italian LOFAR IT computing infrastructure supported and operated by INAF, and by the Physics Department of Turin University (under an agreement with Consorzio Interuniversitario per la Fisica Spaziale) at the C3S Supercomputing Centre, Italy.

This research made use of ASTROPY, a community-developed core PYTHON package for astronomy (Astropy Collaboration et al. 2013) hosted at http://www.astropy.org/, of MATPLOTLIB (Hunter 2007), of APLPY, an open-source astronomical plotting package for PYTHON hosted at http://aplpy.github.com/, and of TOPCAT and STILTS (Taylor 2005).

The National Radio Astronomy Observatory is a facility of the National Science Foundation operated under cooperative agreement by Associated Universities, Inc.

The Legacy Surveys consist of three individual and complementary projects: the Dark Energy Camera Legacy Survey (DECaLS; Proposal ID #2014B-0404; PIs: David Schlegel and Arjun Dey), the Beijing-Arizona Sky Survey (BASS; NOAO Prop. ID #2015A-0801; PIs: Zhou Xu and Xiaohui Fan), and the Mayall z-band Legacy Survey (MzLS; Prop. ID #2016A-0453; PI: Arjun Dey). DECaLS, BASS, and MzLS together include data obtained, respectively, at the Blanco telescope, Cerro Tololo Inter-American Observatory, NSF's NOIRLab; the Bok telescope, Steward Observatory, University of Arizona; and the Mayall telescope, Kitt Peak National Observatory, NOIRLab. The Legacy Surveys project is honoured to be permitted to conduct astronomical research on Iolkam Du'ag (Kitt Peak), a mountain with particular significance to the Tohono O'odham Nation.

NOIRLab is operated by the Association of Universities for Research in Astronomy (AURA) under a cooperative agreement with the National Science Foundation.

This project used data obtained with the Dark Energy Camera (DECam), which was constructed by the Dark Energy Survey (DES) collaboration. Funding for the DES Projects has been provided by the U.S. Department of Energy, the U.S. National Science Foundation, the Ministry of Science and Education of Spain, the Science and Technology Facilities Council of the United Kingdom, the Higher Education Funding Council for England, the National Center for Supercomputing Applications at the University of Illinois at Urbana-Champaign, the Kavli Institute of Cosmological Physics at the University of Chicago, Center for Cosmology and Astro-Particle Physics at the Ohio State University, the Mitchell Institute for Fundamental Physics and Astronomy at Texas A&M University, Financiadora de Estudos e Projetos, Fundacao Carlos Chagas Filho de Amparo, Financiadora de Estudos e Projetos, Fundacao Carlos Chagas Filho de Amparo a Pesquisa do Estado do Rio de Janeiro, Conselho Nacional de Desenvolvimento Cientifico e Tecnologico and the Ministerio da Ciencia, Tecnologia e Inovacao, the Deutsche Forschungsgemeinschaft and the Collaborating Institutions in the Dark Energy Survey. The Collaborating Institutions are Argonne National Laboratory, the University of California at Santa Cruz, the University of Cambridge, Centro de Investigaciones Energeticas, Medioambientales y Tecnologicas-Madrid, the University of Chicago, University College London, the DES-Brazil Consortium, the University of Edinburgh, the Eidgenössische Technische Hochschule (ETH) Zurich, Fermi National Accelerator Laboratory, the University of Illinois at Urbana-Champaign, the Institut de Ciencies de l'Espai (IEEC/CSIC), the Institut de Fisica d'Altes Energies, Lawrence Berkeley National Laboratory, the Ludwig Maximilians Universität Munchen and the associated Excellence Cluster Universe, the University of Michigan, NSF's NOIRLab, the University of Nottingham, the Ohio State University, the University of Pennsylvania, the University of Portsmouth, SLAC National Accelerator Laboratory, Stanford University, the University of Sussex, and Texas A&M University.

BASS is a key project of the Telescope Access Program (TAP), which has been funded by the National Astronomical Observatories of China, the Chinese Academy of Sciences (the Strategic Priority Research Program 'The Emergence of Cosmological Structures' Grant # XDB09000000), and the Special Fund for Astronomy from the Ministry of Finance. The BASS is also supported by the External Cooperation Program of Chinese Academy of Sciences (Grant # 114A11KYSB20160057), and Chinese National Natural Science Foundation (Grant # 11433005).

This project, and the Legacy Survey project, make use of data products from the Near-Earth Object Wide-field Infrared Survey Explorer (*NEOWISE*), which is a project of the Jet Propulsion Laboratory/California Institute of Technology. *NEOWISE* is funded by the National Aeronautics and Space Administration.

The Legacy Surveys imaging of the DESI footprint is supported by the Director, Office of Science, Office of High Energy Physics of the U.S. Department of Energy under Contract No. DE-AC02-05CH1123, by the National Energy Research Scientific Computing Center, a DOE Office of Science User Facility under the same contract; and by the U.S. National Science Foundation, Division of Astronomical Sciences under Contract No. AST-0950945 to NOAO.

DATA AVAILABILITY

Data are available through https://lofar-surveys.org/.

REFERENCES

Antonucci R., 1993, ARA&A, 31, 473
Antonucci R., 2011, preprint (arXiv:1101.0837)
Assef R. J. et al., 2013, ApJ, 772, 26
Astropy Collaboration, 2013, A&A, 558, A33
Baldwin J. A., Phillips M. M., Terlevich R., 1981, PASP, 93, 5
Best P. N., Heckman T. M., 2012, MNRAS, 421, 1569
Best P. N., Ker L. M., Simpson C., Rigby E. E., Sabater J., 2014, MNRAS, 445, 955
Best P. N. et al., 2023, MNRAS, 523, 1729
Blanton M. R., Roweis S., 2007, AJ, 133, 734
Boquien M., Burgarella D., Roehlly Y., Buat V., Ciesla L., Corre D., Inoue A. K., Salas H., 2019, A&A, 622, A103
Brienza M. et al., 2017, A&A, 606, A98
Bruzual G., Charlot S., 2003, MNRAS, 344, 1000
Calistro Rivera G., Lusso E., Hennawi J. F., Hogg D. W., 2016, ApJ, 833, 98
Calistro Rivera G. et al., 2024, A&A, 691, A191
Chabrier G., 2003, PASP, 115, 763
Chilufya J., Hardcastle M. J., Pierce J. C. S., Croston J. H., Mingo B., Zheng X., Baldi R. D., Röttgering H. J. A., 2024, MNRAS, 529, 1472
Chilufya J., Hardcastle M. J., Pierce J. C. S., Drake A. B., Baldi R. D., Röttgering H. J. A., Smith D. J. B., 2025, MNRAS, 593, 463
Condon J. J., 1984, ApJ, 287, 461
Condon J. J., 1989, ApJ, 338, 13
Das S. et al., 2024, MNRAS, 531, 977
Dawson K. S. et al., 2016, AJ, 151, 44
Drake A. B. et al., 2024, MNRAS, 534, 1107
Duncan K. J., 2022, MNRAS, 512, 3662
Dunlop J. S., Peacock J. A., 1990, MNRAS, 247, 19
Euclid Collaboration, 2025, A&A, 693, A250
Fanaroff B. L., Riley J. M., 1974, MNRAS, 167, 31P
Foreman-Mackey D., Hogg D. W., Lang D., Goodman J., 2013, PASP, 125, 306
Gürkan G., Hardcastle M. J., Jarvis M. J., 2014, MNRAS, 438, 1149
Gürkan G. et al., 2018, MNRAS, 475, 3010
Gürkan G. et al., 2019, A&A, 622, A11
Hardcastle M., 2018a, Nat. Astron., 2, 273
Hardcastle M. J., 2018b, MNRAS, 475, 2768
Hardcastle M. J., Croston J. H., 2020, New A Rev., 88, 101539
Hardcastle M. J., Alexander P., Pooley G. G., Riley J. M., 1998, MNRAS, 296, 445
Hardcastle M. J., Evans D. A., Croston J. H., 2007, MNRAS, 376, 1849
Hardcastle M. J. et al., 2016, MNRAS, 462, 1910
Hardcastle M. J. et al., 2019, A&A, 622, A12
Hardcastle M. J. et al., 2023, A&A, 678, A151
Hickox R. C. et al., 2009, ApJ, 696, 891
Hickox R. C., Myers A. D., Greene J. E., Hainline K. N., Zakamska N. L., DiPompeo M. A., 2017, ApJ, 849, 53
Hine R. G., Longair M. S., 1979, MNRAS, 188, 111
Hunter J. D., 2007, Compu. Sci. Eng., 9, 90
Kauffmann G., Heckman T. M., Best P. N., 2008, MNRAS, 384, 953
Kondapally R. et al., 2021, A&A, 648, A3
Kondapally R. et al., 2022, MNRAS, 513, 3742
Kormendy J., Ho L. C., 2013, ARA&A, 51, 511
Lacy M. et al., 2020, PASP, 132, 035001
Laing R. A., Riley J. M., Longair M. S., 1983, MNRAS, 204, 151
Lilly S. J., Longair M. S., 1984, MNRAS, 211, 833
Lyke B. W. et al., 2020, ApJS, 250, 8
Mandal S. et al., 2021, A&A, 648, A5
Marin F., Antonucci R., 2016, ApJ, 830, 82
Mauch T., Sadler E., 2007, MNRAS, 375, 931
Mingo B., Hardcastle M. J., Croston J. H., Dicken D., Evans D. A., Morganti R., Tadhunter C., 2014, MNRAS, 440, 269
Mingo B. et al., 2016, MNRAS, 462, 2631
Morabito L. K. et al., 2022, A&A, 658, A1
Morabito L. K. et al., 2025, MNRAS, 536, L32
Mostert R. I. J. et al., 2024, A&A, 691, A185
Mullin L. M., Riley J. M., Hardcastle M. J., 2008, MNRAS, 390, 595
Narayan R., Yi I., 1995, ApJ, 452, 710
Njeri A. et al., 2025, MNRAS, 537, 705
Novak M., Smolčić V., Schinnerer E., Zamorani G., Delvecchio I., Bondi M., Delhaize J., 2018, A&A, 614, A47
Oei M. S. S. L. et al., 2023, A&A, 672, A163
Oei M. S. S. L. et al., 2024, Nature, 633, 537
Orr M. J. L., Browne I. W. A., 1982, MNRAS, 200, 1067
Panessa F., Baldi R. D., Laor A., Padovani P., Behar E., McHardy I., 2019, Nat. Astron., 3, 387
Pracy M. B. et al., 2016, MNRAS, 460, 2
Prescott M. et al., 2016, MNRAS, 457, 730
Prescott M. et al., 2018, MNRAS, 480, 707
Radcliffe J. F., Barthel P. D., Garrett M. A., Beswick R. J., Thomson A. P., Muxlow T. W. B., 2021, A&A, 649, L9
Readhead A. C. S. et al., 2024, ApJ, 961, 242
Reines A. E., Volonteri M., 2015, ApJ, 813, 82
Rocca-Volmerange B., Le Borgne D., De Breuck C., Fioc M., Moy E., 2004, A&A, 415, 931
Sabater J. et al., 2019, A&A, 622, A17
Sabater J. et al., 2021, A&A, 648, A2
Schmidt M., 1968, ApJ, 151, 393
Shimwell T. W. et al., 2017, A&A, 598, A104
Shimwell T. W. et al., 2022, A&A, 659, A1
Siewert T. M. et al., 2020, A&A, 643, A100
Smith D. J. B. et al., 2016, in Reylé C., Richard J., Cambrésy L., Deleuil M., Pécontal E., Tresse L., Vauglin I.eds, SF2A-2016: Proceedings of the Annual meeting of the French Society of Astronomy and Astrophysics. p. 271 preprint (arXiv:1611.02706)
Smolčić V. et al., 2017, A&A, 602, A2
Stern D. et al., 2012, ApJ, 753, 30
Tasse C. et al., 2021, A&A, 648, A1
Taylor M. B., 2005, in Shopbell P., Britton M., Ebert R.,eds, Astronomical Society of the Pacific Conference SeriesVol. 347, Astronomical Data Analysis Software and Systems XIV, Astronomical Society of the Pacific, San Francisco,. p. 29
Wang Y. et al., 2024, A&A, 685, A79
Whittam I. H., Riley J. M., Green D. A., Jarvis M. J., 2016, MNRAS, 462, 2122
Whittam I. H. et al., 2022, MNRAS, 516, 245
Williams W. L., Röttgering H. J. A., 2015, MNRAS, 450, 1538
Williams W. L. et al., 2018, MNRAS, 475, 3429
Willott C. J., Rawlings S., Blundell K. M., Lacy M., Eales S. A., 2001, MNRAS, 322, 536
Willott C. J., Rawlings S., Jarvis M. J., Blundell K., 2003, MNRAS, 339, 173
Wilman R. J. et al., 2008, MNRAS, 388, 1335
Yue B. H. et al., 2024, MNRAS, 529, 3939
Yun M. S., Reddy N. A., Condon J. J., 2001, ApJ, 554, 803

APPENDIX A: DESCRIPTION OF THE CATALOGUE

We release the full catalogue of 963 764 classified sources with flux density > 1.1 mJy and known redshift with this paper. It can be downloaded from https://lofar-surveys.org/dr2_release.html.

The catalogue consists of the following entries for each source:

(i) All entries from the optical ID catalogue of H23.

(ii) All entries from the catalogue of D24, including optical emission-line fluxes and probabilistic classifications, for those sources for which SDSS data is available. A Boolean column `ELC` indicates objects which have these entries.

(iii) All entries from the SDSS DR16 quasar catalogue, for those sources whose optical position matches a DR16 quasar. A Boolean column `DR16Q` indicates objects that have these entries.

(iv) Flux densities in Jy and spectral indices to allow the *WISE* absolute magnitude to be calculated (`flux_w1`, `flux_w2`, `flux_w3`, `alpha_w1_w2`, `mu` (distance modulus), `alpha_w2_w3`, and `abs_w3`.

(v) Boolean flags `SF_EXCLUDE_BROAD`, `SF_EXCLUDE`, `RQQ_EXCLUDE_BROAD`, `RQQ_EXCLUDE`, `AGN_NARROW` and `AGN_BROAD` which correspond to the classifications summarized in Table 1, with the 'broad' exclusion classifications corresponding to the 'exclusive' classifications in that table.

The RLAGN catalogue used for the analysis in Section 4 can be generated from this catalogue by taking `AGN_BROAD== True`.

Code used to create these catalogues and make the plots in this paper is available on GITHUB at https://github.com/mhardcastle/agn-selection. The data described in this paper constitute version 1.0 of the catalogue, but we plan to update both the DR2 optical ID catalogue and the *WISE*-classified RLAGN/SFG catalogue as further redshifts (and hence, in some cases, additional members of the sample) become available from DESI and WEAVE in the coming years.

APPENDIX B: DEALING WITH OPTICAL LIMITS ON THE LUMINOSITY FUNCTION

Construction of the luminosity functions required the calculation of both radio and optical volumes, $V_{\rm max}$, within which a source could be observed. For the majority of the sources, the optical/near-IR detection limit provided the most constraining factor for the source volume determination, and the considerations involved in this process are discussed here.

Prior to construction of the luminosity functions, a *WISE* Band 1 mag detection limit of $W1 < 21.2$ mag was imposed on the sample to ensure completeness, with the corresponding flux density determining the detection limit for a RLAGN host galaxy. For a given source, this set the maximum redshift out to which it would still be observable ($z_{\rm max}$) and the corresponding maximum volume of the observed sky area enclosed ($V_{\rm max}$), as required for the luminosity function calculations.

In addition to the reduction of flux density expected with increasing source distance, determination of $z_{\rm max}$ required the redshift dependence of the portion of the SED observed in the $W1$ bandpass to be considered. This latter factor is important, since the cosmological K-correction in the $W1$ spectral region of a typical galaxy is negative for the range of redshifts covered by our sample, meaning that higher flux-density spectral regions would be observed at higher redshifts.

To account for this redshift dependence, we first used the KCORRECT code (Blanton & Roweis; 2007; available on GITHUB at https://github.com/blanton144/kcorrect) to obtain rest-frame SED templates for the RLAGN based on their observed DESI Legacy Survey g, r and z optical magnitudes and their *WISE* Band 1 magnitudes; *WISE* Band 2 and 3 mag were also used, when available, to constrain the template fit. Using these templates, the integrated fluxes in the spectral region covered by the $W1$ bandpass were then calculated at increasing redshifts from the target redshift outward. The ratios of these integrated fluxes relative to the target redshift values were then used as correction factors when calculating the predicted higher redshift source flux densities. After also accounting for the increasing cosmological distance, $z_{\rm max}$ and $V_{\rm max}$ values were then determined via comparison of these flux densities with the imposed $W1$ detection limit.

APPENDIX C: EXAMPLE IMAGES OF 'HIGHLY VARIABLE' SOURCES

To investigate the extreme end of the variability of the VLASS counterparts of optical IDs discussed in Section 4.5, we made cutouts of sources with the highest variability indices for visual inspection. Examples of these are shown in Fig. C1. Because these are chosen to be extreme, we would expect some of them to be spurious, and indeed we see one example of a clearly incorrect ID in the catalogue (ILTJ103731.40 + 351839.4, where the alleged optical ID position lies outside the source and in the sidelobes of a bright hotspot), one with a surprising though possibly correct ID position and no clear VLASS core (ILTJ181845.00 + 354243.0) and one where the core position, though correct, is contaminated by a sidelobe of a bright hotspot (ILTJ073509.41 + 344642.4). However, all the others seem to have a clear VLASS detection at the optical ID position and no reason to doubt the genuineness of the variability detection. The majority are morphologically normal FRIIs but it is interesting that two winged sources and one restarting object are among them. 7/12 of these objects, and 7/9 of the ones where we can be confident of the variability detection, are classified as quasars on the basis of their *WISE* colours.

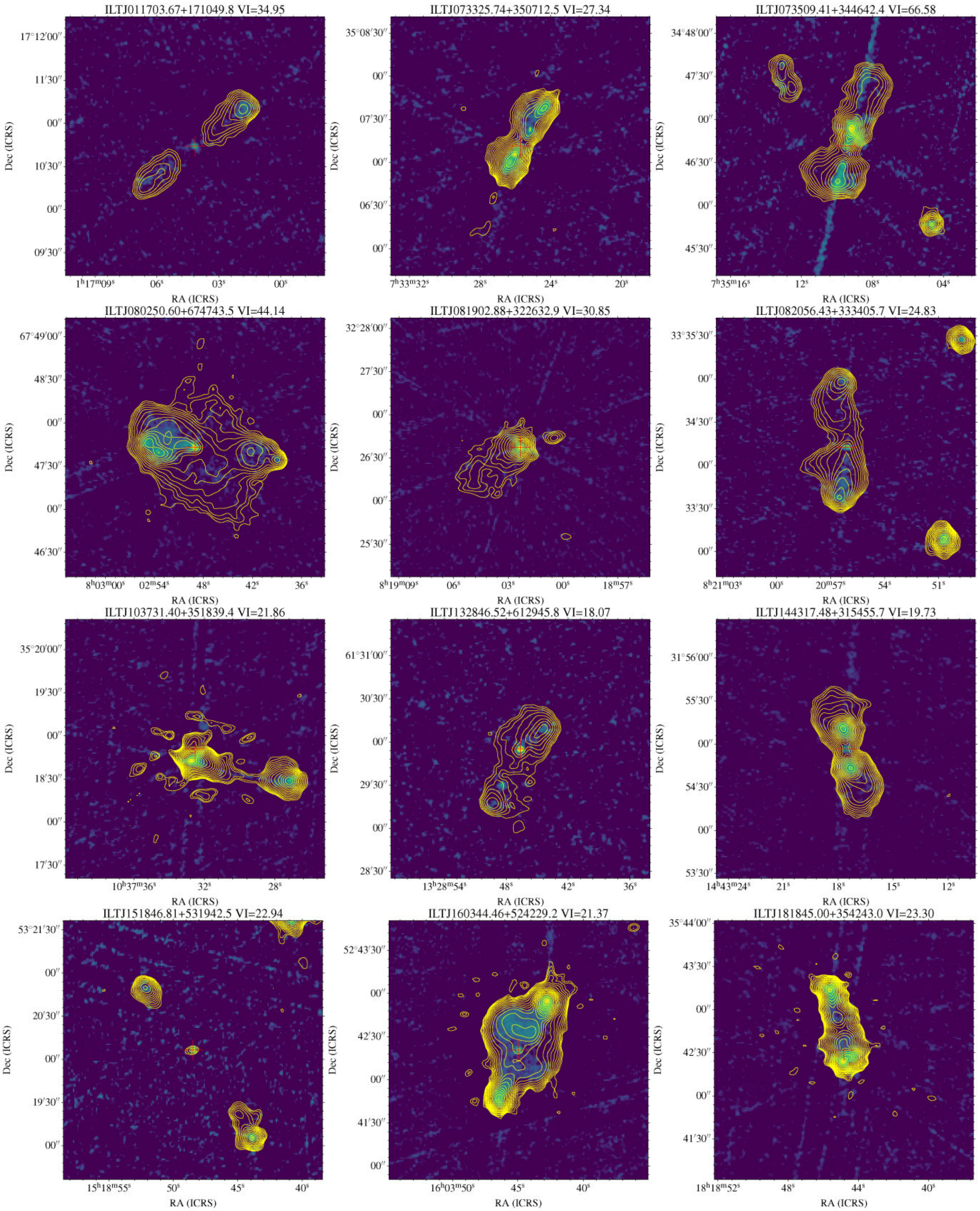

Figure C1. The 12 sources with the largest variability indices as described in Section 4.5. LOFAR contours (increasing logarithmically in steps of 2 from 5σ or peak flux/1000, whichever is the larger) are overlaid on a stacked VLASS colour scale. The red cross indicates the optical ID position. Variability indices (VI) are stated in the title for each image.

This paper has been typeset from a TEX/LATEX file prepared by the author.